AD NUMBER

AD911513

NEW LIMITATION CHANGE

TO

Approved for public release, distribution unlimited

FROM

Distribution authorized to U.S. Gov't. agencies only; Test and Evaluation; APR 1973. Other requests shall be referred to Air Force Avionics Laboratory, Attn: TEM, Wright-Patterson AFB, OH 45433.

AUTHORITY

AFAL ltr, 3 Feb 1976

AFAL-TR-73-72

MICROWAVE FILTERS AND DELAY LINES

W. L. Bongianni, D. M. Heinz and L. Needham
Electronics Group of North American Rockwell

TECHNICAL REPORT AFAL-TR-73-72

April 1973

Air Force Avionics Laboratory
Air Force Systems Command
Wright-Patterson Air Force Base, Ohio

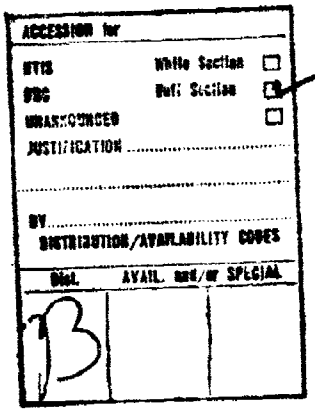

NOTICE

When Government drawings, specifications, or other data are used for any purpose other than in connection with a definitely related Government procurement operation, the United States Government thereby incurs no responsibility nor any obligation whatsoever, and the fact that the government may have formulated, furnished, or in any way supplied the said drawings, specifications, or other data, is not to be regarded by implication or otherwise as in any manner licensing the holder or any other person or corporation, or conveying any rights or permission to manufacture, use, or sell any patented invention that may in any way be related thereto.

Copies of this report should not be returned unless return is required by security considerations, contractual obligations, or notice on a specific document.

(18) AFAL (17) TR-73-2

(14) AD772-585/5ØI

MICROWAVE FILTERS AND DELAY LINES

W. L. Bongianni, D. M. Heinz and L. Needham

FOREWORD

This report on contract F33615-72-C-1760 was prepared by the Advanced Device Technology Department under Peter J. Hagon. This department is part of the Physical Sciences Department in the Research and Technology Division, North American Rockwell Electronics Group.

The contract was initiated under Project 4460, "Solid State Development Technology," Task 446007, "Integrated Microwave Circuits," and was administered by the Air Force Avionics Laboratory, Wright-Patterson Air Force Base, Ohio, with Mr. Russell W. Runnels (AFAL/TEM) as project engineer. The report covers the period 8 May 1972 to 29 December 1972. The contractor's report number is C72-585/501.

The authors would like to acknowledge the significant contributions made by E. Grubb and J. E. Mee.

This report was submitted by the authors April 1973.

"Publication of this report does not constitute Air Force approval of the report's findings or conclusions. It is published only for the exchange and stimulation of ideas".

WILLIAM J. EDWARDS
Chief, Radar and Microwave Technology Br
Electronic Technology Division
Air Force Avionics Laboratory

ABSTRACT

The significance of this research and development to the Air Force derives from the need for small, lightweight solid state integrated circuit devices suitable for signal processing applications at microwave frequencies. The work covered by this report was directed specifically at such devices operating at X band (8.0 to 12.4 GHz). The performance improvement was accomplished by improving the quality of epitaxial YIG films, increasing the knowledge of magnetostatic wave propagation in dielectric layered structures, and utilizing high energy product samarium cobalt magnets. During the period covered by this contract several devices were built and evaluated. These were:

1. A nondispersive delay line at 8.425 GHz with a delay of 125 nsec, an insertion loss of 20 dB, and a bandwidth of 45 MHz

2. A dispersive delay line operating at 9.1 GHz with a 300 MHz linear dispersion of 175 nsec of differential delay. This device compressed a linear chirp by a factor of 30:1 and weighted the adjacent sides lobes to -20 dB

3. A two tap delay line having a nondispersive delay of 50 nsec and 80 nsec.

The success of these devices in terms of size and operating frequency represent a considerable increase in the state of the art. For the first time, the rf signal designer has the opportunity to perform signal processing at radar signal frequencies, with devices which are compatible with Gunn and IMPATT solid state signal sources.

CONTENTS

Section		Page
I.	Introduction	1
	1. Technical Background	2
	2. Objectives	2
	a. YIG Film Quality	2
	b. Samarium Cobalt Magnets	2
	c. Dielectric Layered Structure	2
II.	Film Fabrication	3
	1. Background	3
	2. Substrates	3
	a. Bulk Imperfections in Substrate Wafers	4
	b. Surface Imperfections in Substrate Wafers	6
	3. Epitaxial Film Growth	7
	a. Chemical Vapor Deposition	7
	b. Liquid Phase Epitaxy	12
	4. Epitaxial Film Characterization	14
III.	Film Evaluation	18
	1. Magnetic Wave Propagation Loss	18
	2. Propagation Loss Measurements on Rough Films	20
	3. Epitaxial Growth Rings and Their Effect on Linewidth	21
	4. Propagation Loss on Flux Grown YIG	26
	5. Power Saturation in Flux Grown YIG	30
	6. Cumulative Table of Film Quality	31
	7. Conclusions on Film Quality	31
IV.	Samarium Cobalt Magnets	34
	1. Permanent Magnet Field Strength and Field Uniformity	34
	2. Permanent Magnet Task	34
	3. General Magnet Design Considerations	34
	4. Magnet Field Strength Measurements	35
	a. Proposal Configuration - Single Magnet	35
	b. Single Magnet-Measured Across Poles Parallel to X-Axis	35
	c. Single Magnet-Measured Across Poles Parallel Y-Axis	35
	d. Dual Magnets - Measured Between Poles Parallel Y-Axis	39
	e. Dual Magnets on Laminated Silicon Iron Sub-Yoke	39
	f. Dual Magnets on External Laminated Silicon Iron Yoke	39

CONTENTS (Cont)

Section		Page
	g. Dual Magnets on External 1018 Steel Yoke-Field Shaping	39
	h. Triple Magnet on External 1018 Steel Yoke-Field Variation	40
	i. Cruciform Magnet Configuration	40
	j. Triple Magnet Deliverable Device	40
	k. Five Magnet-Twin Channel Device	47
	5. Machining and Handling	47
	6. Summary	47
V.	X-Band Devices	56
	1. X-Band Nondispersive Delay Line	56
	2. X-Band Dispersive Delay Line	63
	3. Specifications on DDL-EY-3	68
	References	69

ILLUSTRATIONS

Figure		Page
1.	X-ray Diffraction Topograph and Stress Patterns in a (111) Substrate Wafer	5
2.	Iridium Inclusion and Strain Pattern Revealed in a Substrate Wafer by Transmitted Polarized Light with Analyzer Set at Extinction	6
3.	Lack of Stress Patterns Revealed in a Recent (111) Substrate Wafer by Transmitted Polarized Light with Analyzer Set at Extinction	7
4.	YIG Film Grown on GGG Substrate Which Contained Mechanical Damage	8
5.	YIG Film Grown Over Poorly Cleaned Substrate	8
6.	Schematic of T-Shaped Reaction Chamber for CVD YIG Film Growth	9
7.	Microscopic Particle on CVD YIG Film	11
8.	Schematic of Dipping Apparatus for LPE YIG Film Growth	12
9.	Microscopic Particles on LPE YIG Film	14
10.	Magnetic Domains in LPE YIG Films Showing the Normal Straight Domain Walls of Slow Growth and Curved Domain Walls of Rapid Growth	15
11.	Interference Fringe Pattern of a YIG Film Showing Thickness Uniformity and Mesas Caused by Flux Retention	16
12.	Equivalent Circuit of Resonant Cavity	18
13.	Surface Roughness vs Film Thickness for Low Dislocation Density Airtron GGG	22
14.	Linewidth as Calculated from Propagation Loss	23
15.	Linewidth as a Function of Mechanical Polishing on Sample No. 2771-1	24
16.	Nomarski Interference Photomicrograph of Film After Mechanical Polishing and Chemical Etching	25
17.	Photomicrograph of Mechanically Polished Flux Grown YIG Showing Included Grit (280X)	27
18.	Flux Grown YIG Surface after Flux Polishing for 30 Seconds at 860°C (280X)	27
19.	Detailed View of Surface Damage (55X)	28
20.	90 Second Flux Polish at 860°C (280X)	28
21.	150 Second Flux Polish at 860°C (280X)	29
22.	Detailed View of Scratch and Grit Included Free Surface (55X)	29
23.	Film Quality	33
24.	Magnet Axis Identification	36
25.	Measurement Probe Positions	37
26.	Single Magnet Measured Between Poles Parallel Y Axis	38
27.	Dual Magnets	39
28.	Area for Required Field Uniformity	40
29.	Effects of Field Shaping in Short Direction	41
30.	Effect of Adding Third Magnet	42
31.	Field Variations in Y-Axis	43
32.	Cruciform Magnet Configuration	44
33.	Cruciform Magnet Support	45
34.	Triple Magnet Deliverable Device	46
35.	Five Magnet-Twin Channel Device	48
36.	Magnet Structure for Five Magnet Twin Channel Device	51

ILLUSTRATIONS (Cont)

Figure		Page
37.	Microstrip Circuit on 20 Mil Alumina	56
38.	30 Mil YIG Feed 4.5 cm of Air Line	57
39.	30 Mil Feed with No. 2771-3(2) YIG and 4.5 cm Air Line	58
40.	No. 2771-(2) YIG 3 Mil Coupler, 0.5 cm Spaling, 20 Mil Alumina	60
41.	No. 2771-3(3) YIG	61
42.	No. 2771-3(3) YIG, 3 Mil Coupler, 0.5 cm Spaling, 20 Mil Alumina, (Rubber Grommet Feedthrough Suppression)	62
43.	Dispersive Delay Line Using LPE YIG 10.28 μm Thick (NRA 403B-3)	64
44.	Compression Loop for the X-Band Epitaxial YIG Dispersive Delay Line DDL-EY-3	65
45.	Spectrum of Input Chip	66
46.	Time Domain	66
47.	Side Lobe Level	67
48.	-4 DB Points	67
49.	Chip Spectrum Weighted by the Dispersive Delay Line	68

TABLES

Table		Page
I.	Typical Conditions for the Chemical Vapor Deposition of an Epitaxial YIG Film	9
II.	Typical Conditions for Liquid Phase Epitaxy of an Epitaxial YIG Film	13
III.	Comparison of Properties of YIG Films Grown on Cored and Core Free GGG Substrates	26
IV.	YIG Sample Measured During Contract	32
V.	Comparison of Various Magnet Configurations	55
VI.	Two 10.5 Films at X-Band	59
VII.	Specifications on DDL-EY-3	68

SECTION I

INTRODUCTION

1. TECHNICAL BACKGROUND

This program is a logical continuation of previous work carried out by North American Rockwell Corporation on ARPA and AFAL programs over the past 5 years.

Techniques for epitaxial growth of single crystal yttrium iron garnet (YIG) on nonmagnetic substrates by chemical vapor deposition (CVD) were developed under ARPA Order 807, contract AF33(615)-5244, June 1966-June 1968. This program also resulted in a preliminary theoretical understanding of magnetostatic mode spectra in YIG films with experimental verification.

Work performed on a follow-on program - F33615-69-C-1520, March 1969 to July 1970 - extended this work. Material quality of the films was improved to the point where measured linewidths demonstrated it was comparable to the best bulk material. Significant advances were made in the theory of ferromagnetic resonance and the identification and the control of the resonance modes in the epitaxial films. Device feasibility demonstrations were successfully carried out with the results indicating that a powerful signal processing technology at microwave frequencies (1 to 10 GHz) may result from the epitaxial YIG film approach.

Actual device fabrication was achieved in July 1969 to March 1970 when bandpass and bandsectioning filters were delivered to MIT-Lincoln Labs. These filters were built with low linewidth epitaxial YIG on microstrip substrates under a contract with Lincoln Labs. The performance of these devices was comparable with that achieved in commercial YIG sphere filters.

Signal processing devices were built at S band (2 to 4 GHz) on contract F33615-71-C-1101 during the period 15 November 1970 to 15 July 1971. During this period the use of thin YIG films in a dielectric layered structure was first described. Devices using this mode of propagation consisted of a dispersive delay line and a nondispersive tapped line.

2. OBJECTIVES

The purpose of this program was to obtain microwave signal processing devices using epitaxial YIG films at X band (8.0 to 12.4 GHz). This was to be achieved by: (1) improving the quality of epitaxial films, (2) developing magnetic bias structures of samarium cobalt which were compatible with microwave integrated circuits, and (3) more completely understanding the behavior of thin YIG films in a dielectric layered structure.

A brief discussion of each of these objectives should help to explain their importance to device performance.

a. YIG Film Quality

This determines the propagation loss of the magnetostatic wave. Hence it determines the delay, time-bandwidth product, or bit number that a device will have.

b. Samarium Cobalt Magnets

The magnet bias determines the center frequency of device operation. A 9.0 GHz device requires a bias of about 2300 Oe. Prior to the discovery of samarium cobalt, such a field could not be generated in a small package.

c. Dielectric Layered Structure

In bulk YIG devices the dispersion characteristic is only a function of the internal magnetic field and hence shows only monotonic behavior. In the dielectric layered structure, the thickness of the dielectric and YIG film defines a crossover region where dispersion departs from monotonic behavior. The nonmonotonic dispersion includes a region of zero dispersion, $dt/df = 0$, and regions of inflection, $d^2t/df^2 = 0$. The first of these regions, zero dispersion, means that nondispersive delay can be obtained without complex compensating networks. Hence multitapped lines may be constructed in this region. The existence of an inflection point implies a point of symmetry about which frequency inversion can be used to obtain pulse expansion and pulse compression. Further work was then carried out to define these regions mathematically, verify them experimentally with regard to dispersion and attenuation,and employ them in useful devices.

SECTION II

FILM FABRICATION

1. BACKGROUND

This laboratory has been investigating the growth and properties of epitaxial yttrium iron garnet (YIG) films for use in microwave devices since 1966. In addition to a continuing in-house program, a series of Air Force contracts have supported this work. Through the course of these investigations on epitaxial YIG films, considerable experience was gained in growing films by the chemical vapor deposition process. Early in 1970, the pure YIG composition was modified by the addition of gallium to produce the first epitaxial garnet bubble domain films (Ref 1). The merits of epitaxial bubble domain films were readily apparent so that epitaxial films have become standard in bubble domain work. With the widespread interest in bubble domain memory devices, large scale efforts have been directed toward improving the quality of epitaxial films. As a result: (1) the quality of substrate wafers has been improved significantly, (2) new growth techniques have been developed, and (3) new film evaluation methods have been evolved. During the course of the present contract, we have come full circle so that the improvements developed on bubble domain films have been used to produce better YIG films. In the remainder of this Section we will discuss substrates, film growth and film evaluation.

2. SUBSTRATES

During epitaxial crystal growth, the depositing film copies in detail the surface of the substrate wafer. There are thus a number of requirements on the substrate material which must be met in order for epitaxy to take place. First of all, the crystal symmetries, lattice spacing and thermal expansions of film and substrate must be comparable in order to obtain adherent single crystalline overgrowth. Next, the substrate must be inert to the deposition environment. The substrate crystals must also be capable of being grown in large size with good crystalline quality and uniformity. In addition, the mechanical properties of the substrate material must be such that it may be processed into wafers with flat, polished surfaces. And finally, the substrates should be nonmagnetic so as not to couple to the YIG films.

The best substrate material found for YIG films has been gadolinium gallium garnet (GGG) which meets all of the above requirements. Due to the intense interest in this material as a substrate for bubble domain films, it is now commercially available from two suppliers in the form of as-grown crystals or polished wafers. Since imperfections in GGG substrates are propagated into epitaxial YIG films, defects in substrates will be considered in greater detail. We will first consider growth-induced imperfections and then surface preparation-induced imperfections.

a. Bulk Imperfections in Substrate Wafers

GGG crystals are grown by the Czochralski method wherein a single crystal seed is dipped into molten garnet and slowly withdrawn. Depending on the thermal environment at the solid-melt interface and rates of withdrawal and rotation, slow-growing facets may develop on the end of the growing crystal. For a crystal grown along the <111> direction, three {211} facets may form the tip of the crystal (Ref 2). When the crystal is sliced to form (111) wafers, the trace of the three (211) facets is present as a core which is revealed by X-ray topography, as shown in Figure 1a, to resemble a three-bladed propeller. X-ray rocking curves indicate that this core has a lattice constant about 0.002 Å greater than that of the non-core region (Ref 3). As a result, there is considerable strain associated with the core which is revealed optically by stress-birefringence, as shown in Figure 1b. Figures 1a and 1b are of the same wafer.

Another type of imperfection found in Czochralski-grown crystals is growth striation or banding which results from rotation in an inhomogeneous thermal environment. The X-ray topograph of Figure 1a reveals this defect in a wafer as a series of concentric circles, except in the core region where they are approximately straight and parallel lines. Contrast in an X-ray diffraction topograph is a manifestation of deviation from a perfectly periodic crystal so that the striations indicate changes in lattice parameter (Ref 3). The presence of growth bands is also revealed by chemical etching.

In addition to the core and banding which occur through the length of a crystal, there are localized defects. Microscopic inclusions of iridium metal may occur due to dissolution of the crucible in the molten garnet and reprecipitation in the melt with random capture at the growing crystal interface (Ref 4). Such precipitates generate local high strain fields which are revealed by stress-birefringence, as shown in Figure 2. Under certain conditions of melt composition and growth atmosphere, oxide particles composed of garnet chemical constituents may be incorporated as microscopic inclusions in the garnet crystal (Ref 4). When rapid radial growth occurs, as at the seed end of a crystal, microscopic spherical voids are occasionally introduced which are associated with the rejection of dissolved gas. There are also linear and helical dislocations which are generated by growth conditions or inclusions. Dislocations are revealed by X-ray topography (Ref 5) and etching techniques (Ref 6).

The intense interest in epitaxial bubble domain films prompted the identification of the defects cited above and investigations of their origins. As they degrade the quality of YIG films, the substrate imperfections are also deleterious to this program. A film grown over the core and striations must accommodate the difference in substrate lattice parameters. The effects were most noticeable in YIG films grown early in this program which had variations in thickness that mirrored the intense banding in the substrate. These concentric rings in the film surface interfered with the propagation of magnetostatic surface waves. A microscopic inclusion close enough to the surface of a substrate to produce a high strain region can pin magnetic domain walls in YIG but the effect on the surface wave is not known. A void in the substrate surface produces a pit in the film which interferes with surface wave propagation. Dislocations can pin magnetic domain walls in YIG but their effect on the surface wave is not known. Thus, although the effect that each substrate imperfection has is not known, good quality substrates are necessary for good magnetostatic wave propagation in YIG films.

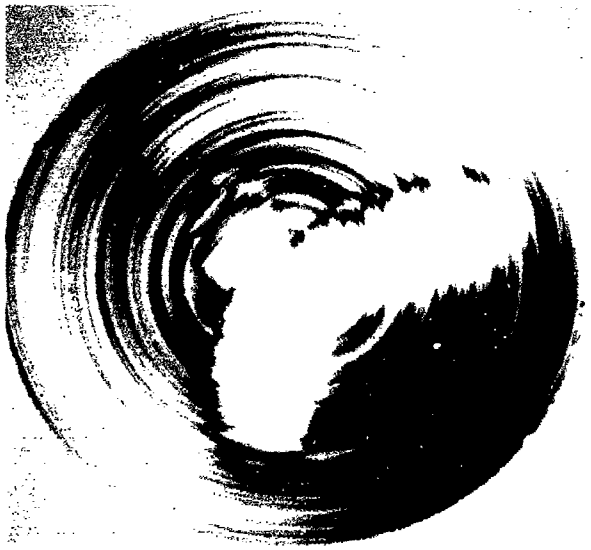

a. X-ray Diffraction Topograph

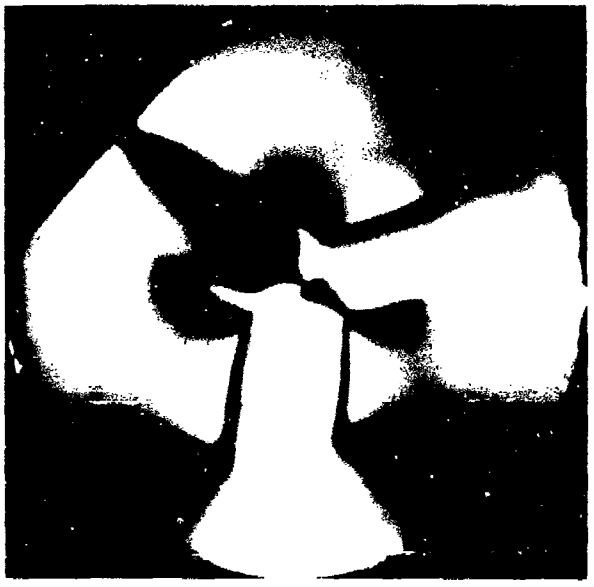

b. Stress Patterns Revealed by Transmitted Polarized Light with Analyzer Set at Extinction

Figure 1. X-ray Diffraction Topograph and Stress Patterns in a (111) Substrate Wafer

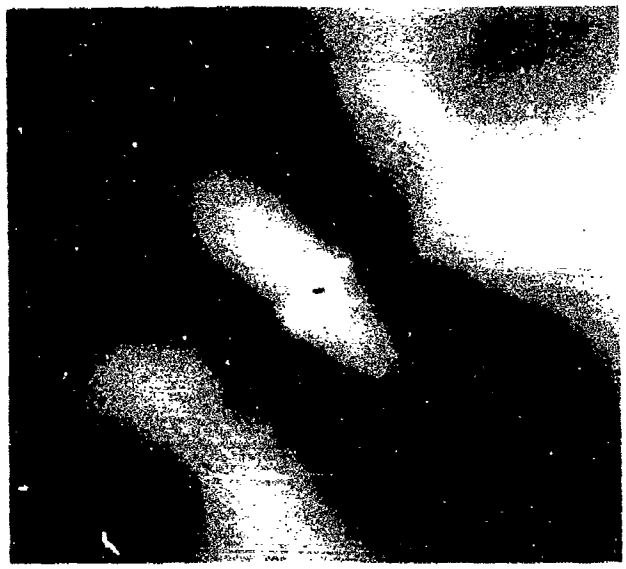

Figure 2. Iridium Inclusion and Strain Pattern Revealed in a Substrate Wafer by Transmitted Polarized Light with Analyzer Set at Extinction

Improved quality GGG became available commercially during the course of this program. Most recently, core-free GGG with medium to low intensity banding, very few precipitates and a low density of dislocations ($\sim 10/cm^2$) has been used for substrates. Figure 3 is a photograph of a substrate taken under the same conditions as Figure 1b. The lack of a core and low intensity banding results in very low stress in the substrate.

b. Surface Imperfections in Substrate Wafers

Since the epitaxial film grows on the surface of the substrate wafer, the surface is as important to the preparation of good films as is the substrate crystal quality. We will therefore consider the surface preparation of substrates next.

After a substrate crystal has been grown, it is ground to a standard diameter: (1) for convenience in processing identical substrates, and (2) for removal of surface irregularities. The cylindrical crystal is next oriented along its <111> axis by an X-ray back-reflection Laue technique and sliced into wafers with a diamond saw. The wafers are then lapped and polished to produce surfaces which are flat and parallel. As a final polish for the epitaxial surface, a colloidal dispersion of silica in an alkaline medium (Syton from the Monsanto Co.) is used. Following polishing, the substrate wafers are cleaned with organic solvents and detergent solutions to remove all traces of the wax which was used to bond the wafer to its polishing block, and to dislodge polishing and dust particles. Substrates may also be subjected to a brief chemical etch in hot phosphoric acid or molten lead oxide flux as a final cleaning measure prior to epitaxial deposition.

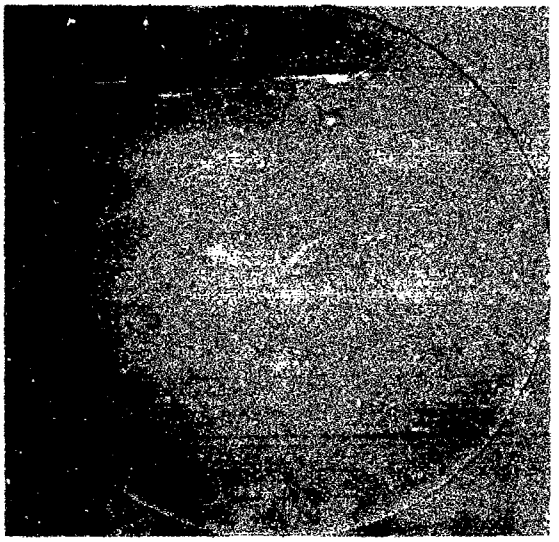

Figure 3. Lack of Stress Patterns Revealed in a Recent (111) Substrate Wafer by Transmitted Polarized Light with Analyzer Set at Extinction

Surface and subsurface scratches produced by mechanical damage during sawing or polishing which have not been completely removed are replicated in the epitaxial film, as shown in Figure 4. Such imperfections are barriers to the movement of magnetic domains in YIG and probably impede the magnetostatic wave. Foreign material such as wax, solvent stains or dust particles on the surface of a substrate act as nuclei so that a film grown over them is not single crystalline, as shown in Figure 5. A magnetostatic wave is scattered by such imperfections. Surface irregularities such as are produced by imperfect mechanical or chemical polishing produce similar irregularities in an epitaxial film; however, if the irregularity is not abrupt, it does not appear to hinder magnetostatic surface waves in YIG films. In summary, substrates with unremoved surface damage or foreign material produce poor YIG films.

Through the course of this program, continually improving substrate surface finishes and the surface cleanliness have been employed as they have been developed on bubble domain programs.

3. EPTIAXIAL FILM GROWTH

YIG films have been grown by chemical vapor deposition (CVD) since the first contract in 1966. Another epitaxial growth method which was developed for bubble domain garnets is isothermal dipping, liquid phase epitaxial (LPE). YIG films have also been grown by this process for this program. A description of the two methods follows, including a discussion of the process variables and limitations of each method.

a. Chemical Vapor Deposition

The CVD process is carried out in a T-shaped reaction chamber, 4 ft wide and 4 ft high, made of 3 in. diameter fused silica tubing, as shown in Figure 6. Anhydrous

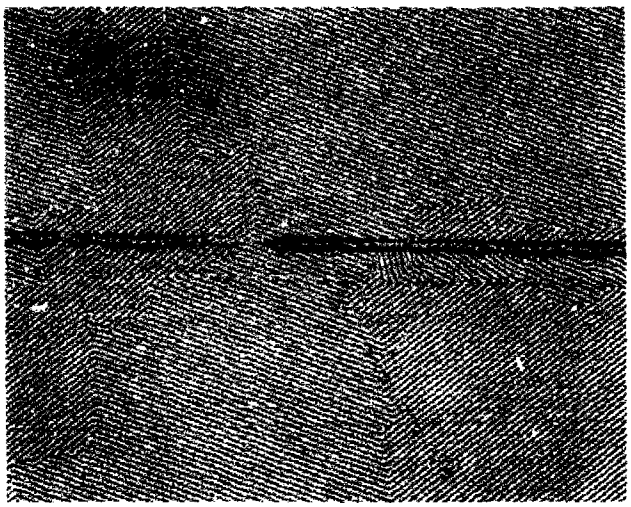

Figure 4. YIG Film Grown on GGG Substrate Which Contained Mechanical Damage

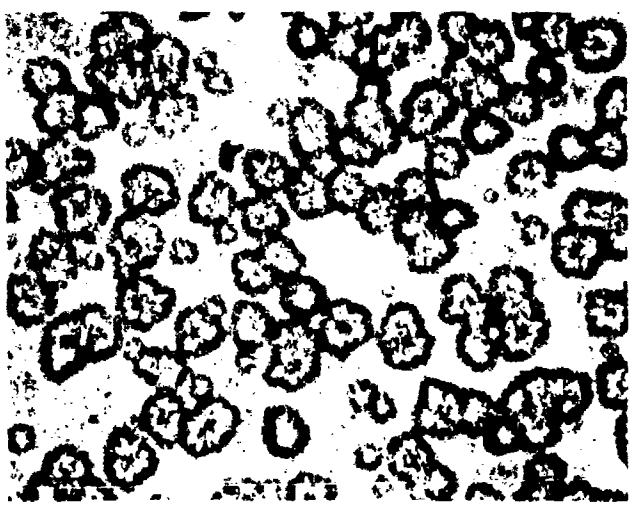

Figure 5. YIG Film Grown Over Poorly Cleaned Substrate

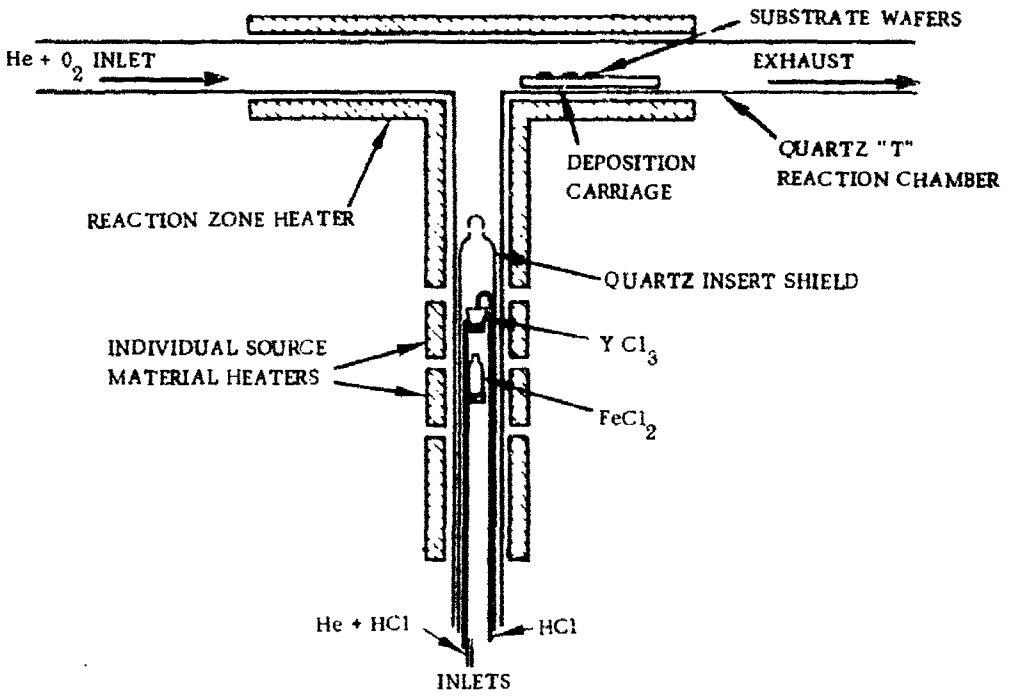

Figure 6. Schematic of T-Shaped Reaction Chamber for CVD YIG Film Growth

iron (II) chloride ($FeC\ell_2$) and yttrium chloride ($YC\ell_3$) are contained in platinum crucibles which are independently heated to control the individual vapor pressures. The vapors mix as they are swept up the vertical portion of the reactor by an inert carrier gas. Oxygen gas, introduced into one horizontal arm of the reactor, reacts with the chloride vapors where they meet to deposit metal oxides downstream on the surface of a substrate at 1100 to 1200°C. Typical gas flow and material transport rates are listed in Table I.

Table I. Typical Conditions for the Chemical Vapor Deposition of an Epitaxial YIG Film

Substrate Temperature	1150°C	Oxygen Flow Rate	58 mℓ/m
Vertical Helium Flow Rate	13.70 ℓ/m	$YC\ell_3$ Transport Rate	1.23 g/hr
Horizontal helium Flow Rate	4.73 ℓ/m	$FeC\ell_2$ Transport Rate	11.6 g/hr
HCℓ Flow Rate	260 mℓ/m	Garnet Deposition Rate	3.82 μm/hr

A characteristic of the CVD process, called the shifting reaction zone (SRZ) behavior (Ref 7), provides a basis for process control. The SRZ is an extension of the thermodynamic reactivity principles which control the chemical reactions. Thus, YIG is not the only product formed in the reactor during a deposition run. Depending on the gas flow conditions and the concentrations of chlorides, O_2 and HCℓ, the possible products include yttrium oxide (Y_2O_3), yttrium orthoferrite ($YFeO_3$), yttrium iron garnet ($Y_3Fe_5O_{12}$) and iron oxides (Fe_2O_3 and Fe_3O_4), or mixtures of these compounds.

In any given run as many as four of these are deposited in or near the seed area. These products appear in a very orderly manner, however, and their order of appearance is consistent with the chemical reactivity of $YC\ell_3$ and $FeC\ell_2$. Thus, because $YC\ell_3$ is considerably more reactive than $FeC\ell_2$, Y_2O_3 is formed first in the reactor, followed by $YFeO_3$, YIG and finally Fe_2O_3. The total reaction zone embracing these products can be shifted from run-to-run, and the individual reaction zones, e.g., the YIG zone, can be shifted or expanded at the expense of the other zones. However, the sequence of deposits is always the same. Additional details and discussion are in Ref 7.

Anhydrous $YC\ell_3$ is obtained from the Lunex Co. of Pleasant Valley, Iowa. It is purified by sublimation in a molybdenum sublimation train at about 1040°C. The anhydrous $FeC\ell_2$ is prepared by direct reaction of iron wire with $HC\ell$ gas. Storage of the anhydrous chemicals is in evacuated containers, while transfer of chemicals into crucibles is performed in a dry box.

In a deposition run, the anhydrous metal halides are loaded into crucibles, weighed, and positioned in separate thermal zones of the reaction vessel. The vaporized halides mix as they rise up the vertical portion of the T-reaction chamber. At the crux of the T, the halides begin reacting with oxygen to produce metal oxides which deposit from the gas stream. Since several products are produced by the reacting chemicals, the growth parameters must be adjusted to maximize the probability of depositing YIG, and minimize the probability of depositing other products in the substrate zone. Using the SRZ concept to adjust chemical ratios and concentrations, the YIG deposition zone may be extended to cover 3.5 inches.

Once the proper conditions have been achieved and stabilized, the seed crystals are pulled into the deposition zone which is located a few inches downstream from the crux of the T. At the conclusion of a deposition period, the seed crystals are withdrawn from the deposition zone. The source chemicals are cooled and weighed to determine use rates.

The color of YIG in thin-film form is dark green so that its presence on a substrate is readily evident. Good films are uniformly smooth (uncrazed) and specularly reflecting. Full circle X-ray diffraction and back-reflection Laue diagrams show the magnetic garnet films to be single crystals which are oriented parallel to the substrates.

Among the process variables for controlling YIG deposition by CVD are the gas flow controls which influence the chemical transport rates and the deposition rate. The source chemical purity also determines the evaporation rate and hence the deposition rate. (Since anhydrous chemicals are involved, any premature reaction with moisture or oxygen reduces the evaporation rate, so that considerable care must be exercised in handling and storing these materials). Individual furnace temperatures control the chemical transport rates and the deposition rate at the substrate. Thus, the process controls for CVD consist of adjusting several gas flows and furnace temperatures as well as maintaining chemical purity.

The major limitations on the CVD growth process are of two types, growth rate and film imperfections. Good quality YIG films can be grown by CVD at from 3 to 6μm/hr, while higher deposition rates may yield facetted rather than flat films or even polycrystalline deposits. As a result of this rate limitation, deposition of a 10 μm YIG film requires from 1.7 to 3.3 hr. A more serious (but related) limitation is caused by imperfections in CVD YIG films which interfere with the propagation of a magnetostatic surface wave. These may be introduced, as indicated earlier, from

imperfections in the substrate material and substrate surface. (CVD growth seems to reproduce substrate surface imperfections more rigorously than LPE growth). In addition, the CVD process can introduce imperfections in the form of microscopic particulate matter which falls on the growing film during the course of the deposition. An example is shown in Figure 7. This particulate matter is probably a reaction product which had deposited on the wall of the silica T upstream of the substrate and then broke away. With care in process control of the deposition, the number of microscopic particles impinging on a substrate can be quite small, but the probability of their occurrence increases with the duration of the run. Thus, during 2- to 3-hr depositions, the number of defects introduced into a YIG film may be so great that an area needed for device work (0.5 cm x 1.0cm), which is free of defects, cannot be found. Thus, at this time, the major restriction on the use of CVD films for magnetostatic surface waves is the number of imperfections.

Another less-understood limitation on the use of CVD YIG is the broader linewidth that is observed. CVD YIG films on GGG substrates and on flux-grown YIG substrates have had linewidths greater than that of flux-grown YIG.

A final limitation is more on the use of GGG as a substrate than on the CVD growth of YIG films. This has to do with lattice constant mismatch wherein GGG has a lattice constant about 0.006 Å greater than that of YIG. Thus, CVD YIG films are in tension, and as the film thickness increases, so does the tension. Thick YIG films craze. This problem may be overcome by using a substrate with a slightly smaller lattice constant such as has been prepared by substituting some dysprosium for gadolinium in GGG. Unfortunately, at this time, the crystal quality of mixed garnets has not been as good as that of GGG. Thus, the preparation of uncrazed 10 to 15 μm YIG films by CVD on GGG is marginal.

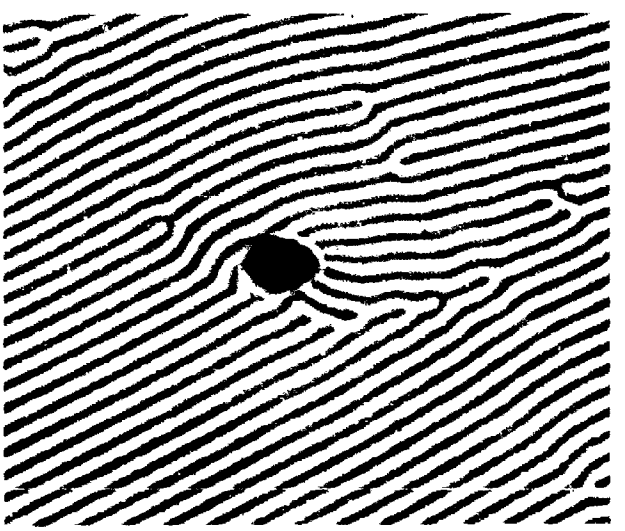

Figure 7. Microscopic Particle on CVD YIG Film

b. Liquid Phase Epitaxy

The epitaxial film growth method which has become standard for bubble domain garnets is isothermal dipping LPE (Ref 8). This process is based on the observation that melts having the appropriate composition of flux and garnet can be supercooled over a large temperature range and remain in the supercooled state, permitting the growth of epitaxial films at constant temperature. A schematic of the equipment used, as shown in Figure 8, consists of a heated crucible containing YIG dissolved in a flux, and a means for dipping a rotating substrate wafer into this melt. Thus, in growing an LPE film, the temperature of the melt is lowered from some holding temperature above saturation to below the saturation temperature. (The greater the supersaturation, the more rapid the growth rate.) The substrate wafer is lowered into the furnace and permitted to equilibrate above the melt to prevent thermal shock. Then the substrate is rotated and lowered into the melt for a predetermined period. Upon withdrawal from the furnace, both surfaces are coated with YIG films. Typical growth conditions are presented in Table II.

The starting chemicals are dried reagent grade Fe_2O_3, B_2O_3, and PbO from the J. T. Baker Co. of Phillipsburgh, N.J., and 99.9 Y_2O_3 from Michigan Chemical Corp. of Chicago, Ill. The chemicals are weighed, ball milled and melted into a 50 mℓ platinum crucible. Next the melt is heated at 1150°C for several hours to equilibrate the solution. The melt is then cooled to 900°C and a substrate is immersed. If no YIG film forms, the temperature is reduced and the process repeated until a film does grow. The saturation temperature is thus bracketed by the temperatures at which a film did and did not form.

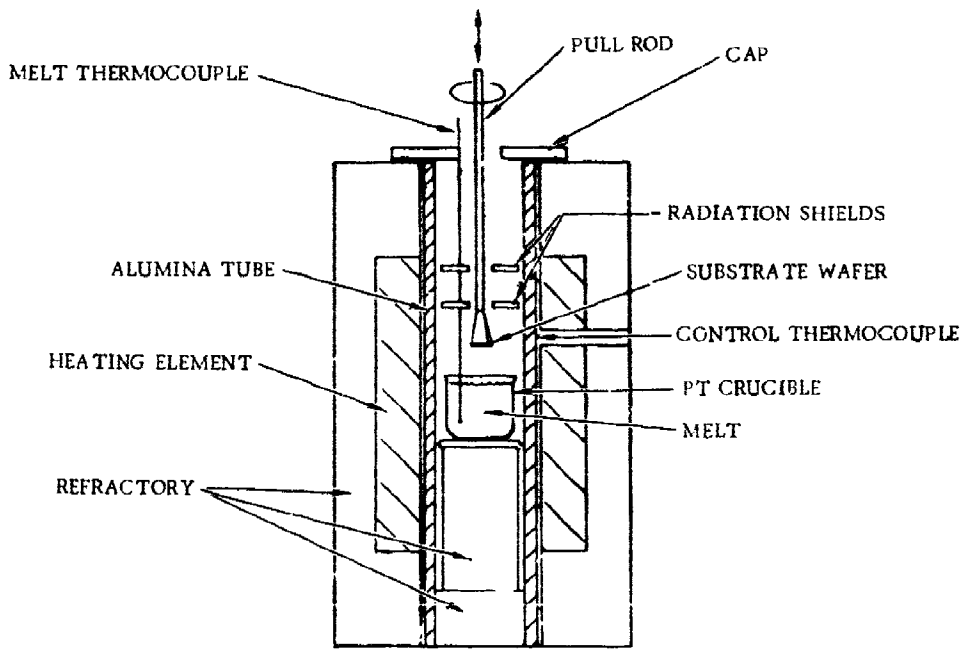

Figure 8. Schematic of Dipping Apparatus for LPE YIG Film Growth

Table II. Typical Conditions for Liquid Phase Epitaxy of an Epitaxial YIG Film

Melt Composition:	Saturation Temperature 891°C
6.38 m. mole Y_2O_3	Growth Temperature 882°C
127.6 m. mole Fe_2O_3	Rotation Rate 17 rpm
80.0 m. mole B_2O_3	Deposition Rate 15.0 μm/hr
1272 m. mole PbO	

The process variables for LPE film growth are fewer in number than for CVD film growth, but all directly influence growth rate and composition. Thus, in choosing an LPE melt composition (Ref 9), the ratio of Y_2O_3 to Fe_2O_3 is selected to minimize the probability of depositing $YFeO_3$ or Fe_2O_3, while the ratio of garnet constituents to flux constituents is selected to minimize the probability of depositing PbO or $PbFe_{12}O_{19}$ and to determine the saturation temperature. Growth of a number of thick YIG films reduces the concentration of garnet in the melt, thereby lowering the saturation temperature. On the other hand, PbO is volatile and is continually being lost from the melt (Ref 10), thereby raising the saturation temperature. Thus, after a melt has been used for some time, the original concentration ratios have been altered. The melt temperature determines the degree of supersaturation and hence the deposition rate (Ref 9). With lower temperature depositions and high deposition rates, lead is incorporated into the garnet film (Ref 11). (The results of the presence of lead in YIG films will be considered later.) Substrate rotation is used to diminish the diffusion path of garnet constituents in the melt to the substrate surface (Ref 12). Thus, the deposition rate increases with rotation rate, but here again, rapid growth increases the lead incorporated into a film. The process variables for LPE growth that are controlled during deposition are thus melt temperature and substrate rotation rate.

As might be expected for different growth techniques, the limitations on the LPE growth process are not the same as those on the CVD growth process. For instance, growth rates for LPE films are two to three times faster than for CVD films so that growth of 10 μm YIG films require only 0.6 to 1.7 hr. One problem with LPE growth which will probably be overcome with an improved substrate holder has to do with flux droplets which adhere to the substrate in the vicinity of the holder. As the substrate is withdrawn from the melt, YIG in these droplets continues to deposit until the droplet solidifies. The flux may be removed with dilute acid but the garnet which deposited remains as a raised area. Such non-uniformities limit the useful areas which may be employed for device work. Another type of limitation is the occasional introduction of microscopic crystallites into an LPE film as shown in Figure 9. The compositions of these imperfections have not been identified as yet but they are probably due to spontaneous nucleation on the surface of the melt. Their presence scatters magnetostatic waves so that they resemble the particulate material in CVD films. The manner in which lead from the flux is incorporated into garnet films is not understood at this time. Its presence may be noted by: (1) the dark brown color of LPE films in contrast with the green CVD films, and (2) the larger lattice constants of LPE films (Ref 11). (This reduces the problem of fitting YIG films on GGG without crazing.) In one YIG film grown quite rapidly, and hence containing more lead than usual, the magnetic domains were round rather than straight-walled as shown in

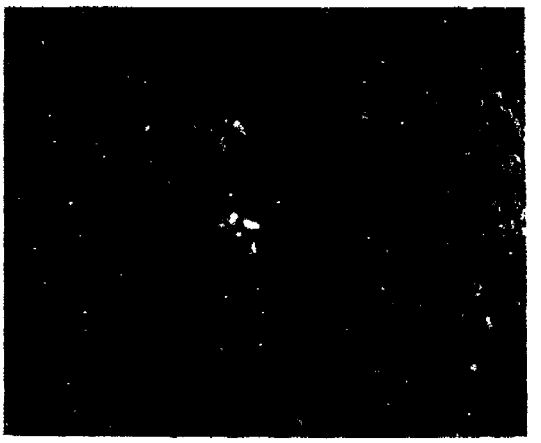

Figure 9. Microscopic Particles on LPE YIG Film

Figure 10, and the ferromagnetic resonance linewidth was too great to be measured (e.g., over 50 Oe). If lead enters the film as Pb^{+2}, replacing Y^{+3}, some charge compensation must take place to produce electroneutrality. One speculation is that an Fe^{+3} becomes and Fe^{-4} but this has not been confirmed. It thus seems desirable to keep the flux ion content of YIG films to a minimum. In summary, the limitations on LPE film growth are not nearly so severe as on CVD film growth; LPE has provided a much better yield of thick, uncrazed YIG film areas of sufficient size for magnetostatic surface wave device work.

4. EPITAXIAL FILM CHARACTERIZATION

Although a variety of characterization techniques have been used on epitaxial YIG films in the past, with the advent of bubble domain devices, a number of new techniques have been developed and made routine. A brief description of the pertinent methods follows.

Once a film has been grown, it is desirable to determine how uniform the layer is. This is routinely done by reflecting monochromatic light from the wafer and photographing the resulting interference fringe pattern. By using the sodium D line in normal incidence to the sample, the fringe-to-fringe spacing corresponds to a film thickness of 0.128μm. Thus, the uniformity of a film may be recorded as shown in Figure 11.

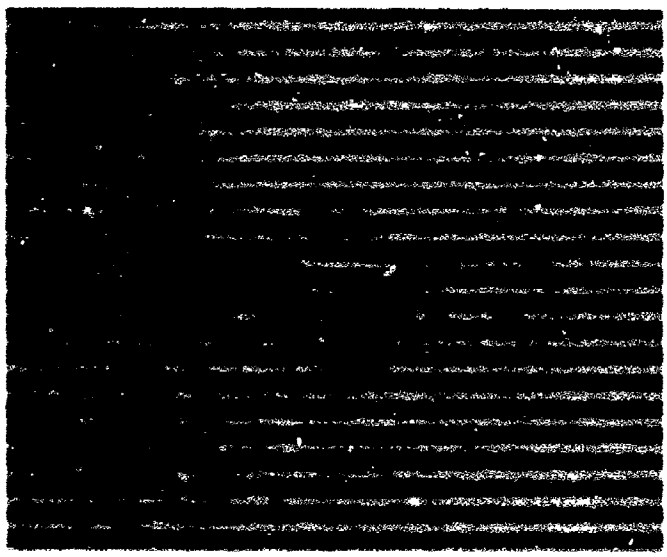

(a) Slowly Grown YIG LPE Film

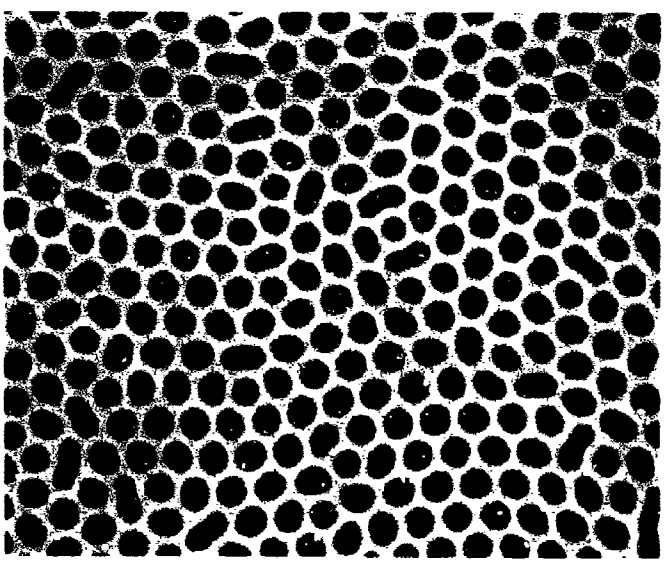

(b) Rapidly Grown YIG LPE Film

Figure 10. Magnetic Domains in LPE YIG Films Showing the Normal Straight Domain Walls of Slow Growth and Curved Domain Walls of Rapid Growth

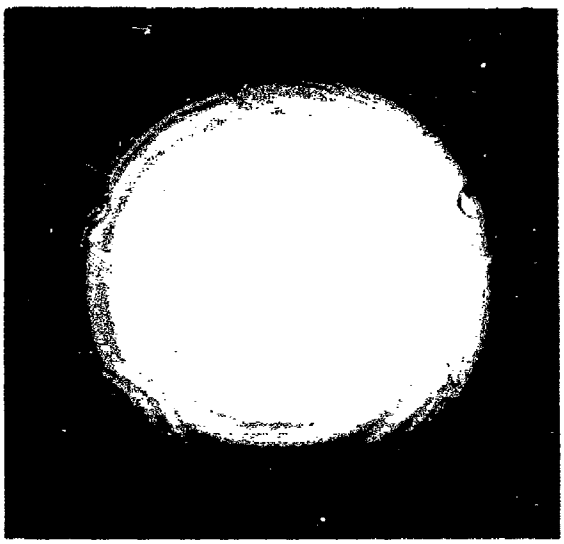

Figure 11. Interference Fringe Pattern of a YIG Film Showing Thickness Uniformity and Mesas Caused by Flux Retention

After observing the thickness variation of the film, a measurement of the thickness is made in an area of the film which shows good uniformity. The measurement is made using a Beckman DK-1A infrared spectrophotometer. For LPE films, the light beam is reflected from the film, while for CVD films, the light is either reflected from the film or transmitted through the substrate and film. In either case, one obtains a trace of an interference pattern which is used to calculate the film thickness.

Under a polarizing microscope, the magnetic domains of YIG are normally revealed as an array of parallel plates, as shown in Figure 10a. When a permanent magnet is brought near, the domains reorient to conform with the magnetic field. If imperfections are present in the YIG film, as in Figures 7 and 9, their presence is made apparent because they pin the magnetic domains. Dark field and Nomarski interference contrast microscopy may be used further to investigate imperfections. By use of transducers on the microscope stage coupled to an x-y recorder, it is possible to prepare a magnified defect map of the film. As the microscope stage is manipulated to follow the edge of the wafer, the pen of the recorder draws the outline of the wafer. Then, focusing on pinning defects or mesas permits them to be drawn on the map. The resulting defect map is about 10 times the wafer size and is conveniently used to identify regions of the film to be cut out for device work. In the course of the magnetostatic surface wave propagation studies, ferromagnetic linewidths are determined. Thus, the characterization measurements determine film uniformity and thickness as well as something about the quality of the film.

In addition to the more routine measurements, certain special measurements are occasionally made. Surface roughness is measured with a Sloan Dektak which may be used with scales ranging from 10^6 Å to 10^3 Å full scale. Lattice constant mismatch between a film and substrate are measured locally by rocking curves using a double crystal X-ray diffractometer (Ref 5) and topographs of the entire wafer are prepared by an asymmetric reflection technique (Ref 5). Film composition may be determined by electron microprobe analysis. As indicated, this group of measurements are only carried out when a situation merits the effort.

At the time this program began, high quality core-free substrates were not readily available and the growth of YIG films was by CVD. Thus these films were strongly influenced by the substrate-induced and growth-induced imperfections. With the improvement in substrate quality as represented by Figure 3, and the growth of YIG films by LPE in the latter stages of the program, the film quality was bettered as represented by Figures 10a and 11 due both to the reduction in substrate-induced imperfections and to the growth technique. Since films were evaluated for utility in devices as they were prepared, a sizable effort was involved in studying the propagation loss associated with CVD film surface roughness. The results of this investigation as well as a comparison with flux-grown bulk YIG and data from the literature are treated in the next section.

SECTION III

FILM EVALUATION

1. MAGNETIC WAVE PROPAGATION LOSS

The minimum propagation loss of a magnetic wave should be the transient decay due to the intrinsic linewidth of the material supporting the wave. That is, propagation decay should be no greater than resonant decay. For example, consider the case of a resonant cavity as shown in Figure 12. The resistance of this circuit is given by:

$$R = R_s (1+\beta_1+\beta_2) , \tag{1}$$

where β_1 and β_2 are the input and output coupling coefficient respectively. The loaded Q is

$$Q_L = \frac{\omega L}{R} = Q_u \left(\frac{1}{1+\beta_1+\beta_2} \right) . \tag{2}$$

If i_o is the electrical current in the circuit at the instant that the signal source is turned off, then the current decays as

$$i(t) = i_o e^{-(R/2L)t} , \tag{3}$$

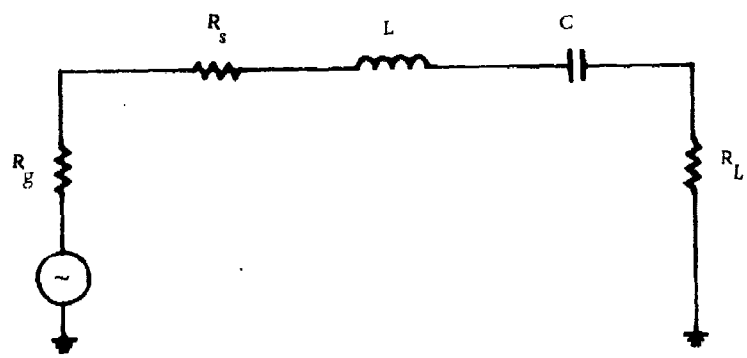

Figure 12. Equivalent Circuit of Resonant Cavity

where the term due to sinusoidal variation is ignored. By substituting in Eq (2) we have

$$i(t) = i_o e^{-(\omega_o/2Q_L)t} \quad . \tag{4}$$

If the current is measured at two successive times, $i(t_1)$ and $i(t_2)$, the ratio of current would be

$$\frac{i(t_1)}{i(t_2)} = e^{-(\omega/2Q_L)(t_1-t_2)} \tag{5}$$

or solving for Q_L

$$Q_L = \frac{\pi f(t_2-t_1)}{\ell n \frac{i(t_1)}{i(t_2)}} \quad . \tag{6}$$

In microwave measurement, signal level ratios, A_s are measured in dB, which are ratios of $10 \log_{10} \frac{i(t_1)}{i(t_2)}$, hence

$$Q_L = \frac{\pi f(t_2-t_1)}{\frac{\log_{10}\left(\frac{i(t_1)}{i(t_2)}\right)}{4.34}} = \frac{4.34\,\pi f(t_2-t_1)}{A} \quad . \tag{7}$$

In the case that the propagating wave loss is considered equal to the internal resonance loss, $Q_L = Q_u$. That is, no energy is lost to the outside world, but is maintained in the resonant structure with its attendant losses. Equation (7) becomes

$$Q_u = \frac{f}{\Delta f} = \frac{4.34\,\pi f(t_2-t_1)}{A} \quad . \tag{8}$$

Since the intrinsic loss is given by ΔH,

$$\frac{1}{\gamma \Delta H} = \frac{4.34\,\pi(t_2-t_1)}{A} \quad . \tag{9}$$

It is now possible to solve this expression for propagation loss α as

$$\alpha = \frac{A}{t_2-t_1} = 4.34\pi\gamma\Delta H$$

or

$$\alpha = 38.2\,\Delta H \ (\text{db}/\mu\text{sec}) \quad . \tag{10}$$

As an example, a 1 Oe linewidth material would have an α of 38.2 dB/μsec. Measurements made on epitaxial YIG for the previous contract, AFAL-TR-71-275, and reported in the literature (Ref 13) quote a figure of 110 dB/μsec and Brundle and Freedman (Ref 14) quote a figure for flux grown bulk YIG of 300 dB/μsec. These figures represent linewidths of 3 Oe and 8 Oe respectively, considerably above the intrinsic linewidth of YIG.

This discrepancy has been solved on bulk grown YIG by Adam (Ref 15). He pointed out that mechanical polishing of the YIG crystal into slabs introduced surface damage that interfered with the propagation of the surface magnetic wave. The surface damage was confined to a layer several microns thick, referred to as the Bilbe layer. Adams removed the Bilbe layer by chemical polishing techniques and measured the propagation loss before and after chemical polish. He found that the original 300 dB/μsec was reduced to 27 dB/μsec after chemical polish. This last figure represents a linewidth of 0.7 Oe which agrees with the intrinsic linewidth of the material.

The slightly lower (110 dB/μsec vs 300 dB/μsec) loss in epitaxial YIG is probably due to the fact that this YIG surface is never mechanically polished, hence no Bilbe layer is present. This figure is still half to one order of magnitude larger than the intrinsic linewidth of epitaxial YIG measured on a previous contract, F33615-69-C-1520, as reported by Besser (Ref 16).

The questions arises - where is the energy going? A similar energy loss in ferrimagnet sphere filters has been investigated by Dionne (Ref 17). He assumed that surface irregularities gave rise to local demagnetizing fields which either damped or scattered energy into higher order spin waves. This phenomenological theory gave rise to the equation

$$\Delta H = \Delta H_{\text{intrinsic}} + A\,(4\pi M_s)\,\frac{\delta}{d}$$

where A is an experimentally determined constant, $4\pi M_s$ is the saturation magnetization, d is the diameter of the sphere, and δ is the depth of the surface irregularity induced demagnetization.

Other sources of loss in epitaxial YIG films are bulk associated. There are substrate induced strain and dislocations, cracks and inclusions grown into the film, and chemical impurity. Fortunately, the effects of strain and dislocations can be minimized by high quality substrates. The rest can be minimized through proper attention to growth procedures. Once this is done, it should be possible to examine the surface contributions to propagation loss in a systematic way.

2. PROPAGATION LOSS MEASUREMENTS ON ROUGH FILMS

A systematic study of YIG films on low defect density GGG has been made. Film thickness, roughness, and magnetic wave propagation loss have been measured for seven samples ranging in thickness from 1.9 μm to 15.5μm. The following observations have been made:

1. The film roughness δ is related to the YIG film thickness d by the relation

$$\delta = kd^{3/2}$$

where $k = 4.75\ m^{-1/2}$. The roughness is concentric about the substrate center and appears to follow growth rings of the substrate. The surface roughness was measured on a Sloan Technology Corporation Dektak surface profile plotter. The results of this series of measurements are shown in Figure 13.

2. The propagation loss gives rise to the linewidth ΔH which varies with thickness as

$$\Delta H = k'd^{-3/2},$$

where $k' = 56 \times 10^{-9}$ Oe.$m^{3/2}$. This relation holds to about 9μm after which the linewidth begins to increase with increasing thickness. The propagation loss was measured using a sampling scope and calibrated attenuator. The readings were taken at a frequency of 3.39 GHz. A plot of the results is shown in Figure 14. By way of comparison, the data given by Adams was processed to yield loss data for the flux grown bulk YIG plates. It is interesting to note that a similar slope is observed.

3. Taking observations (1) and (2) together we arrive at the conclusion

$$\Delta H = \frac{kk'}{\delta}, \text{ where } kk' = 252 \times 10^{-9} \text{ Oe.m.}$$

This result is totally unexpected, implying as it does that linewidth is inversely proportional to roughness and is independent of thickness (up to 9 μm).

3. EPITAXIAL GROWTH RINGS AND THEIR EFFECT ON LINEWIDTH

It has been found that expitaxial YIG films do not grow with a uniformly flat surface, but rather with concentric rings like the rings of a tree or the ripples from a stone thrown into a still pond. The roughness of these rings is easily measured with a surface profile probe and the results of a series of measurement indicates that the roughness is directly related to film thickness.

Since the surface magnetostatic wave is a surface phenomena, it would be expected that the growth rings would have some effect on the propagation. Such an effect was observed. It consisted of reduced attenuation with increased roughness until a critical film thickness was reached, after which the attenuation increased. The improvement in progagation with roughness is a surprising result and an attempt was made to duplicate the results by an alternate procedure.

This procedure consisted of taking a thick epitaxial YIG film and polishing the growth rings down. The original film was sample No. 2771-1, which was a 13.5 μm film grown on a low defect density GGG substrate. An 0.3 μm alumina polishing compound was used to partially polish down the peaks of the rings. Four data points were obtained — at the original 2400Å unpolished roughness, at two intermediate polished roughnesses, and at a completely polished surface. The linewidth was measured for each of these surface conditions and plotted in Figure 15 where a best line fit has been drawn. As can be seen, the linewidth continues to decrease with increasing surface

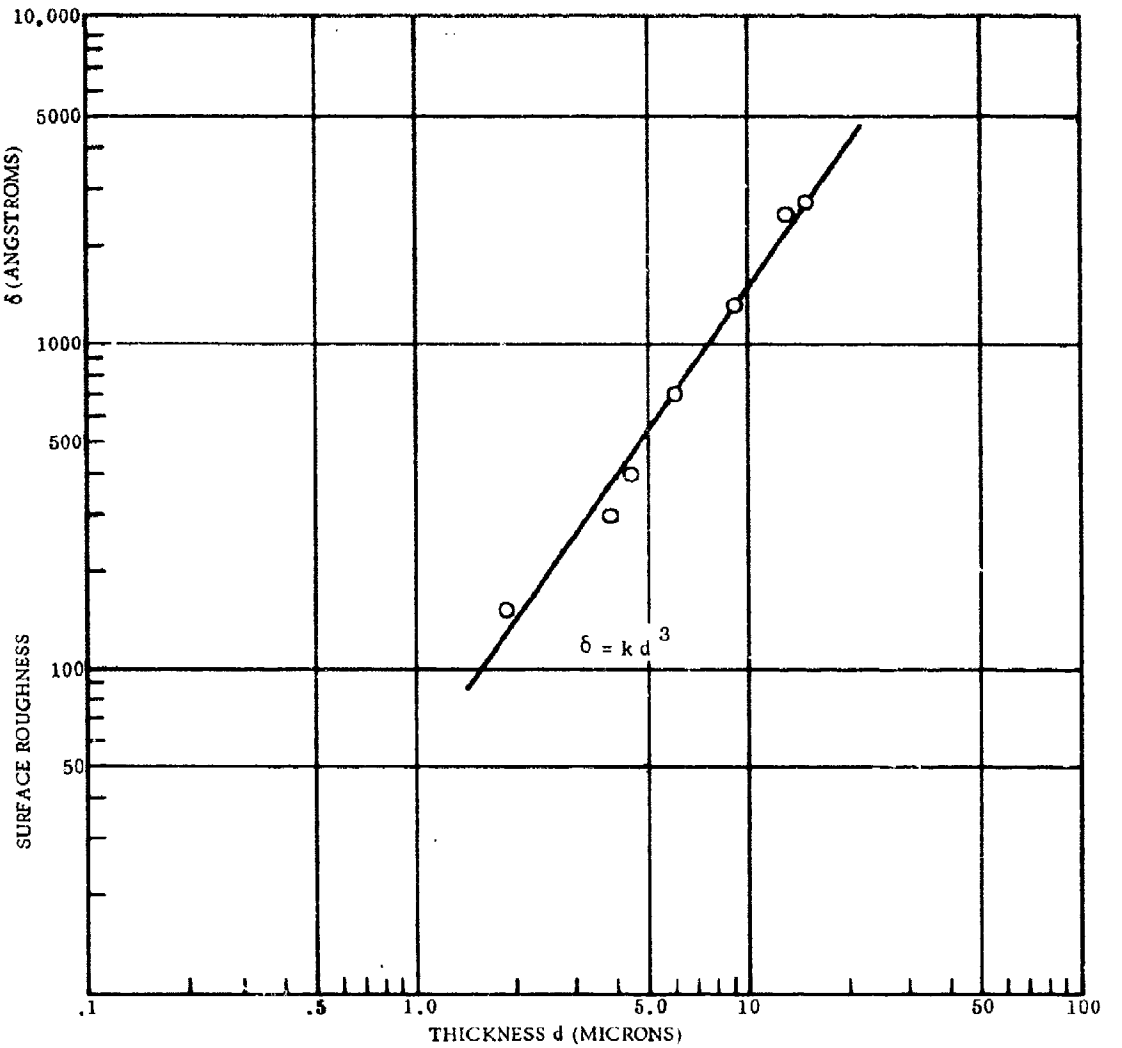

Figure 13. Surface Roughness vs Film Thickness for Low Dislocation Density Airtron GGG

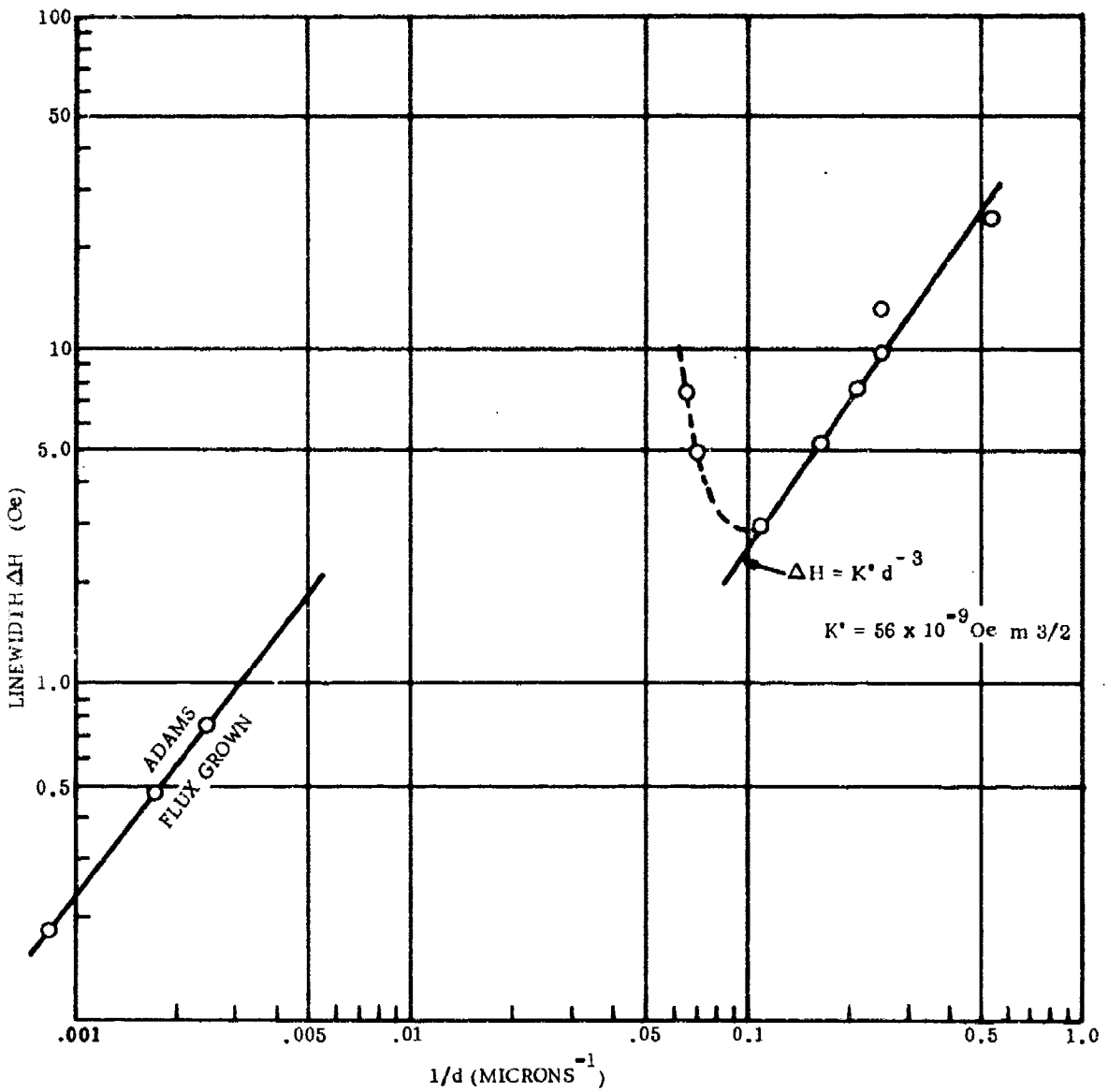

Figure 14. Linewidth as Calculated from Propagation Loss

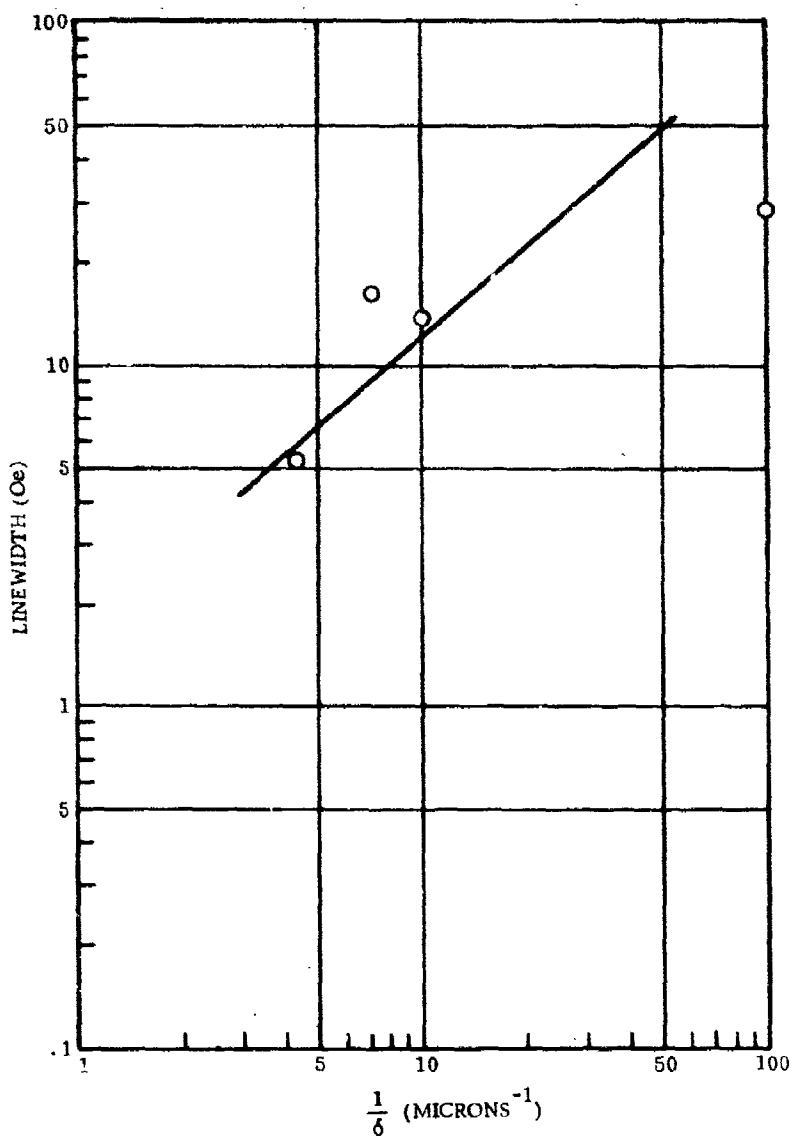

Figure 15. Linewidth as a Function of Mechanical Polishing on Sample No. 2771-1

roughness. After the final polishing, the thickness was remeasured and found to be 12.8 μm. This is too small a thickness variation from the unpolished film to be considered important.

The film was then chemically etched in H_3PO_4 at 105°C for 5 sec and examined for polishing damage under a Nomarski interference contrast microscope. A photomicrograph is shown in Figure 16. The etch pits due to surface damage are clearly visible, and so are the growth rings. A surface profile indicates that the pits are 1500Å deep and the rings are 100Å deep.

The presence of growth rings on the films implies the presence of these rings in the substrate material. Surface profile measurements reveal no rings after mechanical polishing. However, when the substrate is etched the rings appear. Preferential etching of this sort implies local strain in these rings.

When a core is present in a substrate, it is also strained and may be revealed by etching. The strain in such material is large enough to be observed under crossed polarizers as shown in Figure 2. A review of the substrates revealed that core strain was indeed present in Airtron material, but that Linde material was core free. Samples of YIG films grown on cored and core-free substrates were measured by surface profile and propagation loss. The values are compared with expected values for the cored substrates in Table III.

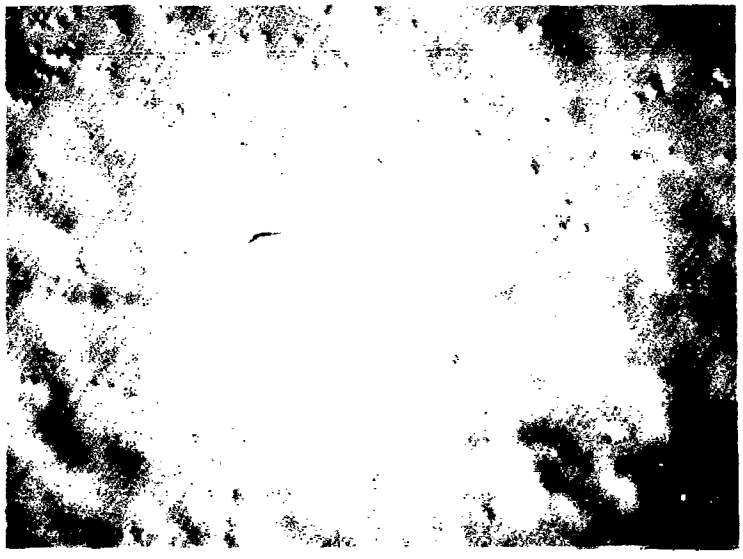

Figure 16. Nomarski Interference Photomicrograph of Film After Mechanical Polishing and Chemical Etching

Table III. Comparison of Properties of YIG Films Grown on Cored and Core Free GGG Substrates

Thickness	Cored (Airtron)		Core Free (Linde)	
	Roughness	Linewidth	Roughness	Linewidth
3.4μ	300Å	10.2 Oe	<25Å	5.4 Oe
10.5μ	1500Å	3.0 Oe	80Å	2.5 Oe

The core free substrate films consistently exhibit a lower linewidth, despite having a lower surface roughness which suggests that the presence of a core in a substrate has a greater influence on the quality of a YIG film than the growth rings.

In summary, this study has shown that CVD YIG films grow with a surface roughness which reflects the growth bands in the substrate: (1) The linewidth of such YIG films decreases with roughness up to a film thickness of 9 μm, beyond which the linewidth increases. (The cause of this behavior is not clear at this time.) (2) Polishing down the roughness of a film thicker than 9 μm causes the linewidth to decrease, and (3) films grown on core free substrates are smoother and have a narrower linewidth than films grown on cored substrates. Thus, core free substrates with a minimum of growth banding are preferable for low linewidth YIG films.

4. PROPAGATION LOSS ON FLUX GROWN YIG

In the previous section, it was concluded that the epitaxial YIG propagation loss was a function of substrate quality and surface condition. For comparison, an initial attempt was made at measuring the properties of flux grown bulk YIG. It was hoped that measurements on this material would provide a standard for epitaxial YIG. In addition, Adam's work would be repeated with the hope of obtaining his 0.7 Oe linewidth for surface wave propagation.

An 82 gram crystal was obtained from Airtron. It was X-ray oriented and [110] plates were sliced from it. Infrared and visual inspection disclosed cracks and microscopic particles of flux inclusion in the plates. The plates were polished with 0.1μm alumina polishing compound (Linde B) and a much higher density of included particles were observed. Since these particles were not originally observed, it was concluded that the particles constitute alumina grit entrapped in the surface. Figure 17 is a microphotograph of the surface -- the included grit is clearly visible. Propagation loss on these samples measured a minimum of 300 dB/μsec with a linewidth of 8 Oe.

Chemical polishing was then accomplished by dipping a sample in PbO flux at 860°C for 30 sec. Figure 18 shows a photograph of the surface at the same magnification as Figure 17. The entrapped particles have been removed but the surface is deeply pitted. A lower power surface photomicrograph, Figure 19 shows a vast network of scratches and other damage which the pitting has outlined.

The sample was then etched an additional 60 sec at 860° for a total of 90 sec. Figure 20 shows that the pits have become wider and begin to overlap. In addition, growth rings, very much resembling the growth rings on epitaxial YIG, have begun to appear. After another minute of flux polishing, Figure 21, the pits have fully overlapped and become shallower. A lower power photograph, Figure 22, shows when

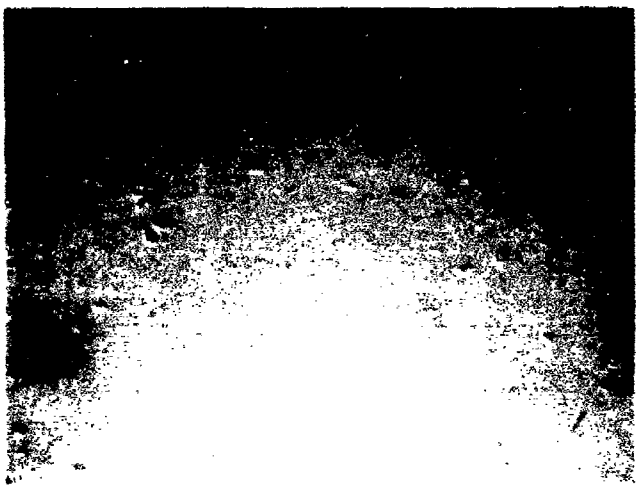

Figure 17. Photomicrograph of Mechanically Polished Flux Grown YIG Showing Included Grit (280X)

Figure 18. Flux Grown YIG Surface after Flux Polishing for 30 Seconds at 860°C (280X)

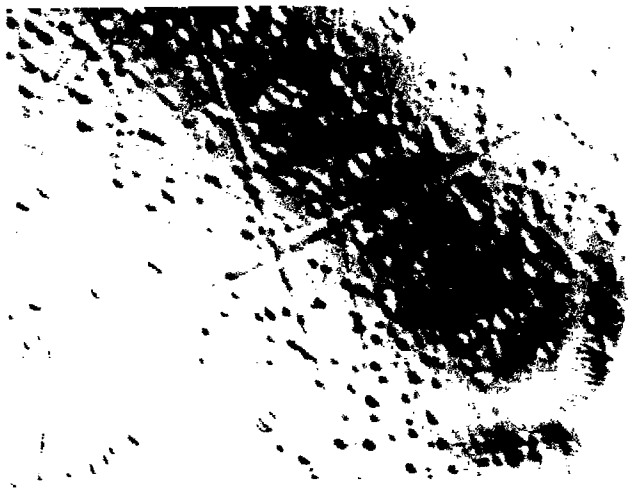

Figure 19. Detailed View of Surface Damage (55X)

Figure 20. 90 Second Flux Polish at 860^{o}C (280X)

Figure 21. 150 Second Flux Polish at 860°C (280X)

Figure 22. Detailed View of Scratch and Grit Included Free Surface (55X)

compared to Figure 17, that all the surface damage introduced by the mechanical polishing has been removed. All that remain are the shallow pits and growth rings.

Two slabs were cut from this polished sample and the linewidths were measured. Both measured 0.7 Oe. Dimensions and linewidth are compared with Adams in the following.

	Thickness	Linewidth
This Study	24.5 mils	0.7 Oe
Adams	22.2 mils	0.47 Oe

The agreement is quite good and is more in line with the expected linewidth of this material. The 0.7 Oe value compares with a best measured value of 2.5 Oe on a 10.5μm thick epitaxial film.

5. POWER SATURATION IN FLUX GROWN YIG

There is presently little doubt that epitaxial YIG films have a significantly greater linewidth than flux grown bulk YIG. Both flux polishing and chemical polishing of YIG slabs yielded the same linewidth when the mechanically damaged layer was removed (2 μm). This linewidth was 0.70 Oe as compared with 2.6 Oe of the best epitaxial film.

Some confusion in measurement occurred at the beginning since the flux grown material saturated at much lower levels of rf power. Once this was understood, measurements became repeatable. In fact, the saturation becomes a secondary proof of the difference in linewidth between flux and epitaxial material. The critical rf field associated with spin wave instability h_{crit} is given by

$$h_{crit} = \left(\frac{\Delta H}{2}\right)\left(\frac{1.54\Delta H}{4\pi M_s}\right)^{1/2}$$

If two samples are found to differ in saturation by a power level P, where

$$P = 20 \log_{10}\left(\frac{h^1_{crit}}{h^2_{crit}}\right) \text{ in dB, then the relative linewidth is}$$

$$\frac{\Delta H_1}{\Delta H_2} = 10^{P/30}$$

In experiments, the difference between epitaxial YIG saturation and flux YIG saturation is ~20 dB, which yields

$$\frac{\Delta H_1}{\Delta H_2} \quad 4.6$$

This is about the ratio measured by direct linewidth measurements.

This result implies that long delay times can only be achieved at the price of lower dynamic range. As a rough estimate, an epitaxial YIG device will have a 74 dB dynamic range as against a bulk YIG device with 54 dB over a 100 MHz bandwidth.

6. CUMULATIVE TABLE OF FILM QUALITY

A cumulative table of CVD films grown for this contract and bulk YIG samples is given in Table IV. It will be noticed that only two films have been grown with a linewidth under 3.0 Oe (115 dB/μsec). While all flux grown bulk YIG slabs have measured considerably less than this, bulk YIG cannot be used to achieve nondispersive behavior. LPE films grown for this program are not included in the table because these films present problems in linewidth evaluation. Since both sides have an LPE film, such a film does not have an unambiguous nondispersive region and hence cannot be measured with the same accuracy as a CVD film. An LPE film could be measured if the film on the other face were removed, however time did not allow measurement by this technique. Device performance, as discussed in Section V, indicated that LPE films performed as well as CVD No. 2771-3(2) which was the best CVD film grown. This is an encouraging situation since LPE films have not had nearly the development effort that CVD and bulk flux materials have had.

7. CONCLUSIONS ON FILM QUALITY

Based on the work during this contract, the surface wave linewidth of epitaxial YIG films is much larger than the intrinsic linewidth of the material. Figure 23 is taken from recent work by Merry and Sethares (Ref 19). The work of both Adams and Merry et. al. is taken on flux grown material with particular attention paid to the quality of surface finish. The top curve is for the epitaxial CVD film No. 2771-3(3). The epitaxial film has a propagation loss about five times greater than bulk flux grown material. There is no inherent reason for this larger loss in epitaxial material, so that with an improved growth process (e.g., liquid phase epitaxy) and improved substrates, it is expected that comparable losses will be achieved — with comparable improvements in device performance.

It is worthwhile to point out that neither bulk flux grown material nor epitaxial material is yet at the limit of performance. Both loss curves go as $f^{1/3}$, whereas the intrinsic linewidth goes as f^1; hence, even further reduction in loss can be expected.

Table IV. YIG Samples Measured During Contract

Film No.	Thickness (Microns)	Surface Roughness	Substrate	Linewidth at 4.0 GHz	Surface Appearance	Comments
No. 2767	5.93	700Å	Cored G^3	5.25 Oe	Growth Rings	
No. 2766	4.43	400A	Cored G^3	7.7 Oe	Growth Rings	
No. 2765	9.23	1300Å	Cored G^3	2.90 Oe	Growth Rings	
No. 2768Y	~3.3	1300Å	YIG	4.6 Oe	Crazed	
No. 2769	3.82	300Å	Cored G^3	9.8 Oe	Growth Rings	
No. 2770A	1.9	~150Å	Cored G^3	24.5 Oe	Smooth	
No. 2770 1B	14.3	3000Å	Cored G^3	6.0 Oe	Growth Rings	
No. 2770 2B	~15	3000Å	LyGdGaG	7.3 Oe	Crazed and Growth Rings	
No. 2771	13.5	2400Å	Cored G^3	5.3 Oe	Growth Rings	
No. 2771-3(1)	10.5		Core Free G^3	6.0 Oe	Scratches	Mechanical Polish Only
No. 2771-3(2)	10.5	~80Å	Core Free G^3	2.5 Oe	Clear with Rings	Flux Polish
No. 2771-3(3)	10.5		Core Free G^3	4.0 Oe	Cloudy	Flux Polish
Bulk Flux YIG #1	620			0.7 Oe	Shallow Pits	Chemical Polish
Bulk Flux YIG #2	700			0.7 Oe	Shallow Craze	Flux Polish
No. 3489	12.5		Core Free G^3	13.0 Oe	Mosaic Cracks	
No. 3488	3.9		Core Free G^3	13.1 Oe	Mosaic Cracks	Flux Etched Substrate
No. 3489	12.5		Core Free G^3	7.9 Oe	Mosaic Cracks	Chemical Etched Substrate
No. 3490	15.9		Core Free G^3	3.8 Oe	Smooth	Film Grown on Wrong Side

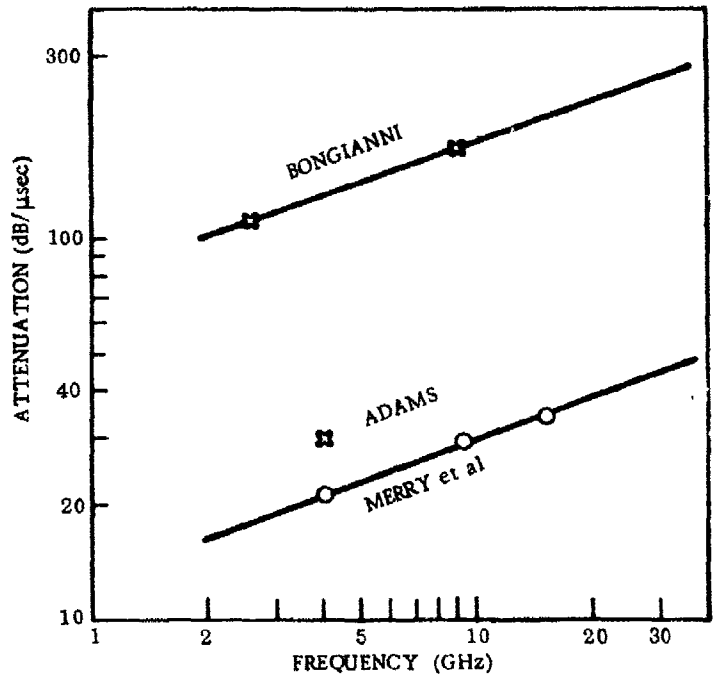

Figure 23. Film Quality

SECTION IV

SAMARIUM COBALT MAGNETS

1. PERMANENT MAGNET FIELD STRENGTH AND FIELD UNIFORMITY

The investigation of magnet configurations and dimensions which lead to a successful X band delay line and a pulse compression filter are described in this section. Magnetic field strength measurements are reported for a series of permanent magnet arrangements, from the single magnet system which was originally proposed through various arrangements of two, three, and four magnets. The final selection was a three magnet system single channel, and a five magnet system dual channel.

2. PERMANENT MAGNET TASK

The contract defined task was to perform the experimental work necessary to relate field strength and field uniformity to the aspect ratios of various samarium cobalt magnets. Calculations showed that field strengths of up to 2.5 kilogauss would be needed. A rugged structure which was small and light was required for airborne application. The entire project was feasible only after the recent introduction of samarium cobalt permanent magnets which have an energy produce ratio of 15K gauss-oersteds (5.6K for the next highest strength magnet, Alnico V). Since the magnet material was new, it would also be necessary to gain experience in handling and machining the samarium cobalt.

3. GENERAL MAGNET DESIGN CONSIDERATIONS

For any permanent magnet, the flux density at the gap B_G is proportional to:

$$\frac{L_M H_d}{L_G}$$

and to:

$$\frac{A_M B_d}{A_G}$$

where

L_M = length of magnet

H_d = magnetizing force

L_G = length of gap

A_M = cross section area of magnet parallel to pole faces

B_d = flux density of magnet at operating point

A_G = area of gap

This shows that for a given air gap the flux density can be controlled by varying the length of the magnet or the cross section area. As a practical limitation magnets were not available longer than 0.93 in.

4. MAGNET FIELD STRENGTH MEASUREMENTS

For uniformity, the axes for the configurations reported here are defined in Figure 24. All field Strength measurements were made with a Hall probe type gaussmeter (RFL Model 1890 serial number 767). Location of the probe relative to the magnet poles were as shown in Figure 25.

a. Proposal Configuration - Single Magnet

The NREG proposal suggested using a single magnet with the YIG located between poles. Several magnets of different dimensions were measured by Method 1 of Figure 25. The highest values obtained, ranged from 0.3 to 0.88 kilogauss immediately at the surface. These readings were far below the required 2.5 kilogauss. Results are shown in Figure 26.

b. Single Magnet-Measured Across Poles Parallel to X-Axis

Values measured using Method 2 of Figure 25 were a little higher than for Method 1, the largest, thickest magnet giving highest field strengths. Measured values were:

	Measurement Location		
Magnet Size	Edge	Center	Edge
0.1 x 0.3 x 0.3 in.	0.48K gauss	0.04K	0.6K
0.1 x 0.6 x 0.6 in.	0.46K	0.05K	0.55K
0.25 x 0.6 x 0.6 in.	1.14K	0.05K	1.24K

└—Across Poles Dimension

c. Single Magnet Measured Across Poles Parallel Y-Axis

Measurements using Method 3, Figure 25 were also made and found to yield even higher values than Method 2. Data received are as follows:

	Measurement Location				
Magnet Size	Edge		Center		Edge
0.1 x 0.3 x 0.3 in.	0.2K gauss	–	1.9K	–	0.45K
0.1 x 0.6 x 0.6	0.5K	1.6K	0.3K	1.6K	0.4K
0.25 x 0.6 x 0.6	0.45K	2.5K	1.5K	2.25K	0.5K

└—Across Poles Dimension

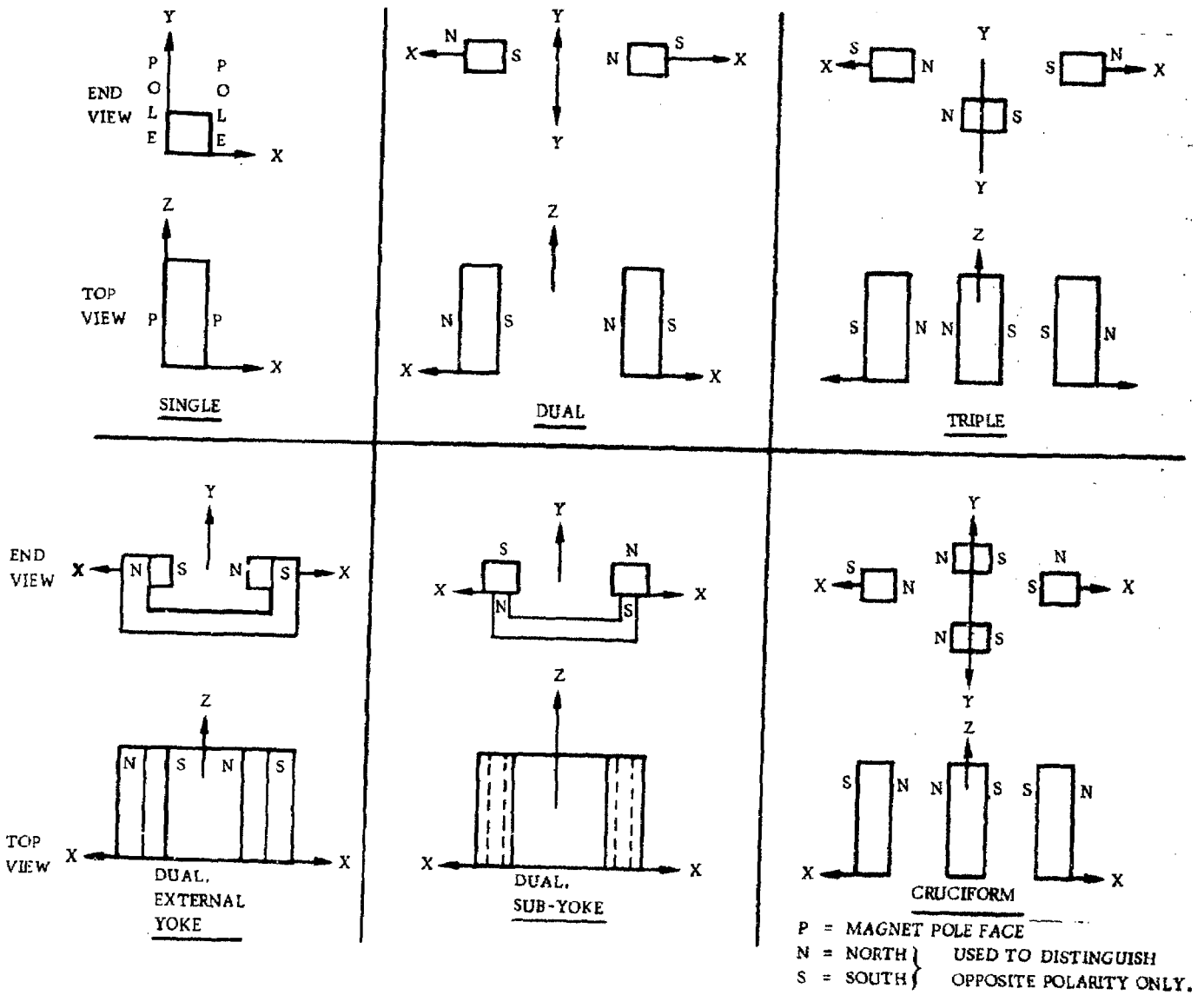

Figure 24. Magnet Axis Identification

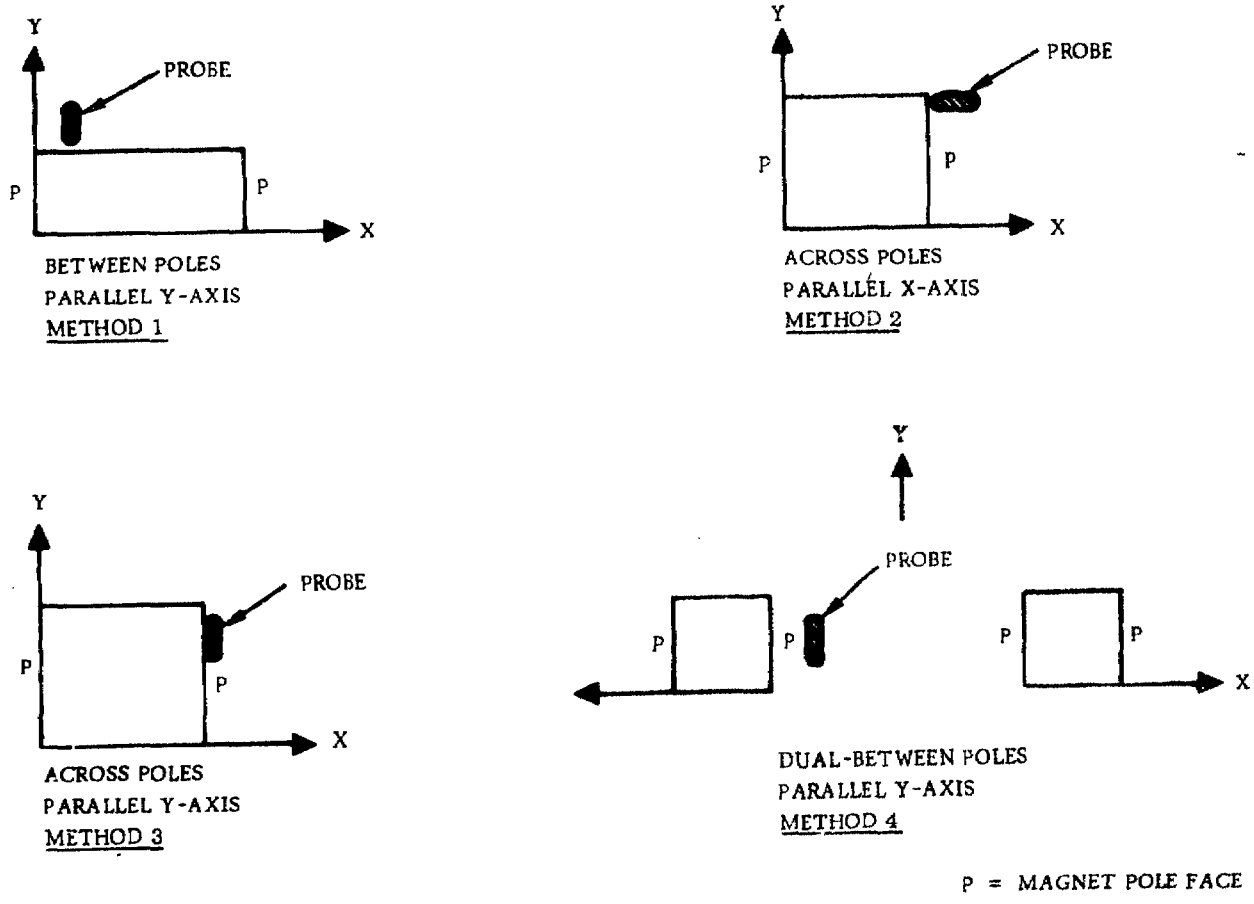

Figure 25. Measurement Probe Positions

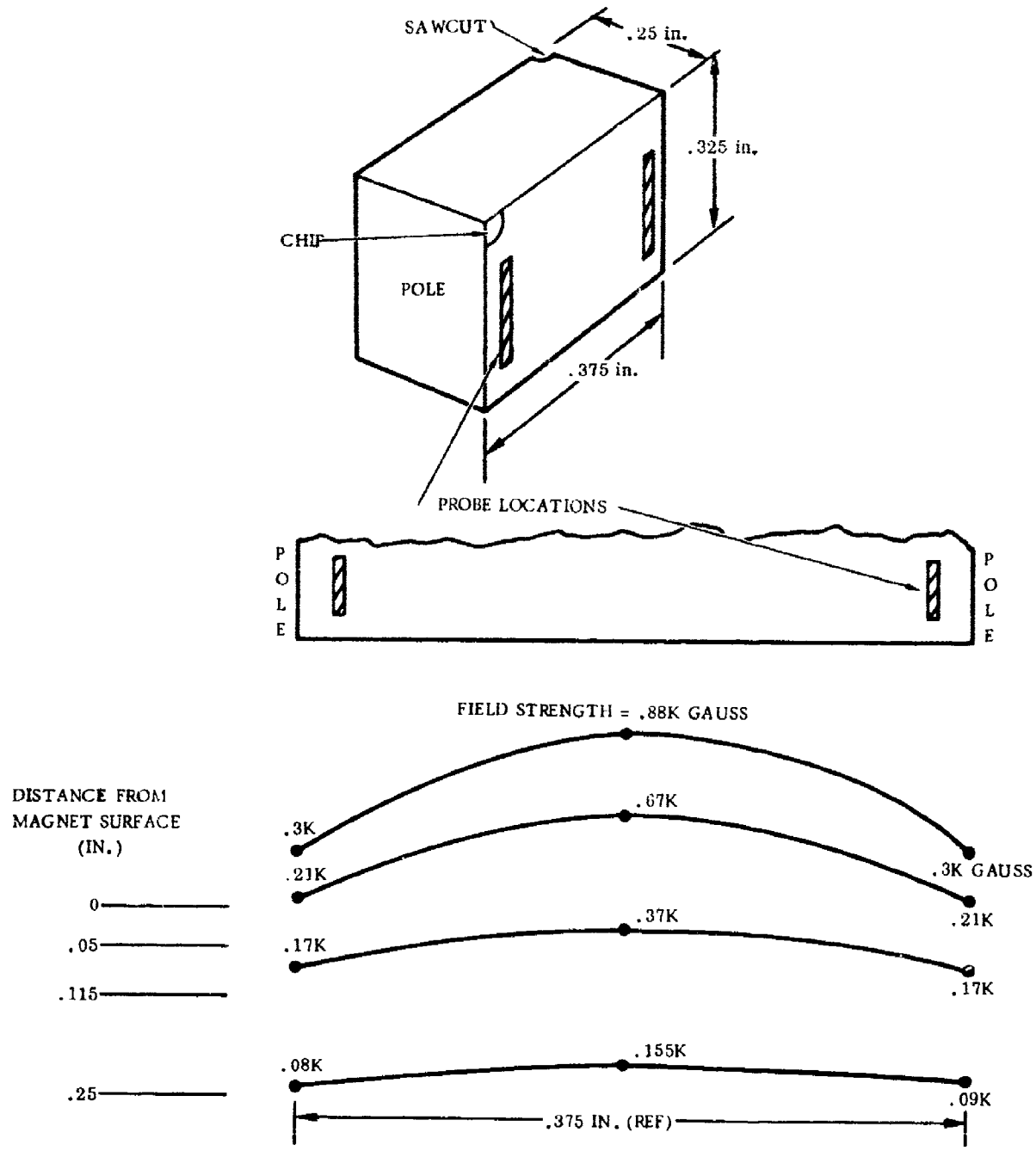

Figure 26. Single Magnet Measured Between Poles Parallel Y Axis

d. Dual Magnets - Measured Between Poles Parallel Y-Axis

Values near the ranges required on this program were obtained using Method 4. Physical dimensions for this measurement are shown in Figure 27 with edge to center to edge readings of 3.6, 1.61, and 2.24 kilogauss respectively.

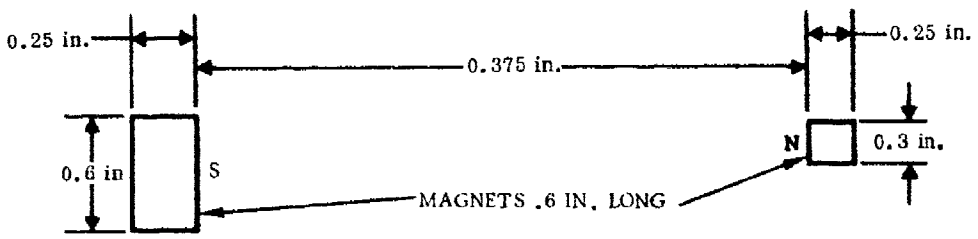

Figure 27. Dual Magnets

e. Dual Magnets on Laminated Silicon Iron Sub-Yoke

Additional measurements on the same magnets as in Para d were made with the magnets mounted on top of a laminated, silicon iron sub-yoke. This approach gives very uniform readings of 1.26, 1.33, 1.22 and 1.3 kilogauss.

A proprietary powder material called ERTIA from AD-Vance R/D Company, Oceanside, California, was also evaluated as a means for showing magnetic lines of force. No useful information emerged from that approach.

At this stage it became evident that field uniformity should be as shown in Figure 28.

f. Dual Magnets on External Laminated Silicon Iron Yoke

The magnets measured in Para d and e were measured on external laminated silicon iron yokes. The measured values were extremely high with readings of 4, 2.35 and 3.8K gauss; however, the fields were not uniform.

g. Dual Magnets on External 1018 Steel Yoke-Field Shaping

Greater field uniformity was achieved in the center with external 1018 steel yokes when the magnet pole faces were ground with a radius in the Y axis. Results are shown in Figure 29.

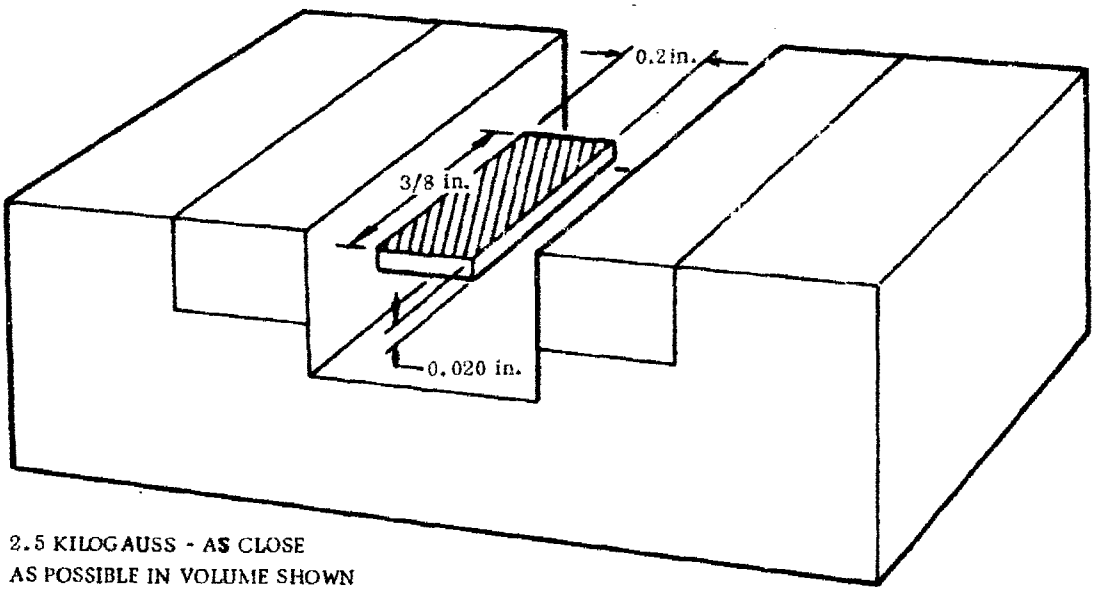

Figure 28. Area for Required Field Uniformity

h. Triple Magnet on External 1018 Steel Yoke-Field Variation in Y Axis

The addition of a third field deflecting magnet, made considerable improvement in uniformity together with high field strengths. The field had significant variations in the Y-axis which proved to have great value in the non-dispersive line. Results of this measurement are shown in Figures 30 and 31.

i. Cruciform Magnet Configuration

In the central portion of the cruciform magnet configurations in that area to be occupied by the YIG as defined in Figure 28, the field was found to be uniform within about 300 gauss (Figure 32). The cruciform magnet support is shown in Figure 33.

A delay line was built using this configuration, but difficulty was encountered in changing YIG substrates and positioning the input and output strip line. When the cap containing the fourth magnet was removed it was possible to produce a functioning delay. The field for this configuration, which is not quite so uniform, is shown in Figure 34.

j. Triple Magnet Deliverable Device

A functioning delay line was produced using three magnets in the lower portion of the cruciform support of Figure 33. The uniformity in the usable area was about 350 gauss, but the level dropped about 500 gauss (Figure 34). Positioning of the YIG and the input/output stripline was extremely critical.

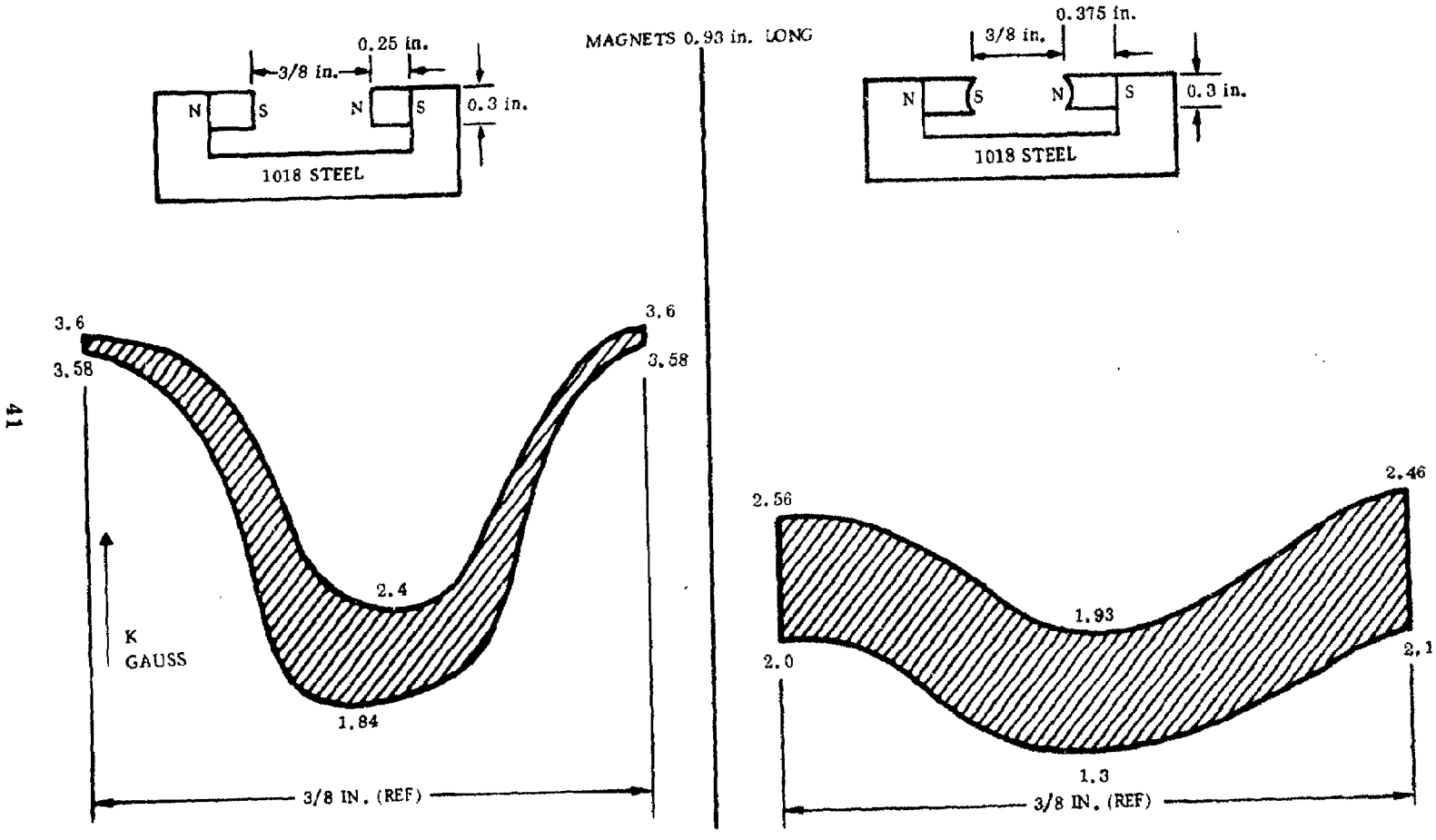

Figure 29. Effects of Field Shaping in Short Direction

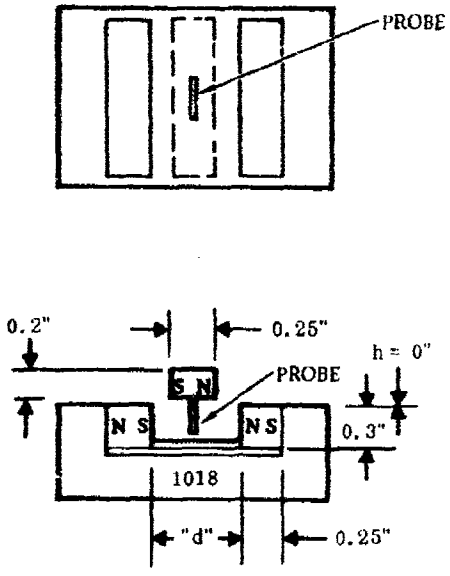

ALL MAGNETS 0.93 IN. LONG

Distance "d" (IN.)	Field Strength (K gauss)	
	Two Magnets Only	With Third Magnet as Shown in Position
0	3.94	3.93
1/8	2.84	3.55
3/16	2.5	3.6
1/4	2.62	3.62
3/8	3.94	3.93

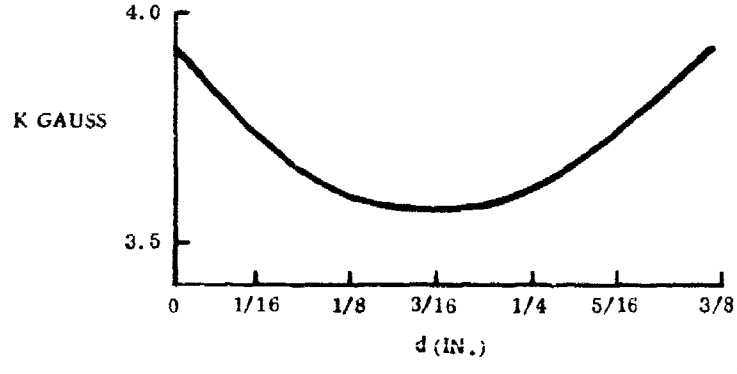

Figure 30. Effect of Adding Third Magnet

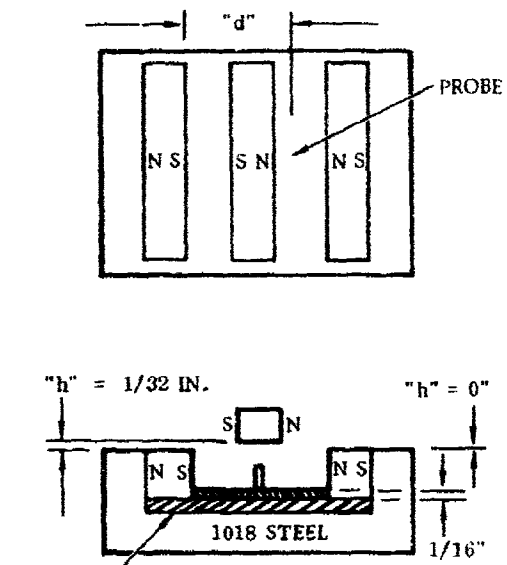

Distance d(IN.)	Field Strength (K gauss)	
	h = 1/32 In.	h = 0
0	3.94	3.94
1/16	3.67	——
1/8	3.33	3.42
3/16	3.23	3.32
1/4	3.25	3.16
5/16	3.45	——
3/8	3.88	3.74

ALL MAGNETS 0.93 IN. LONG
SAME AS FIGURE 30

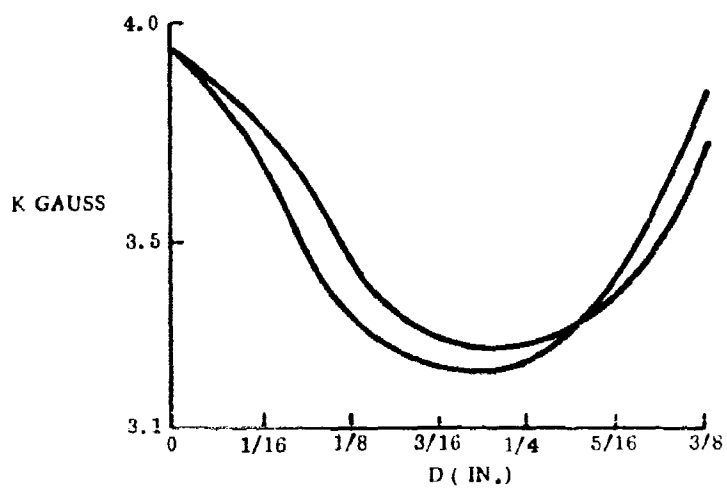

Figure 31. Field Variations in Y-Axis

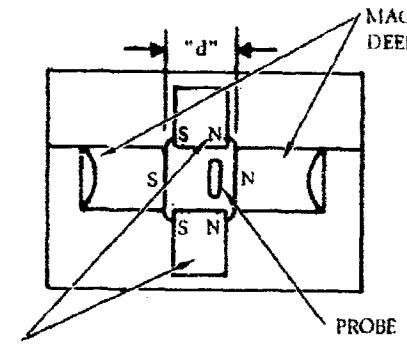

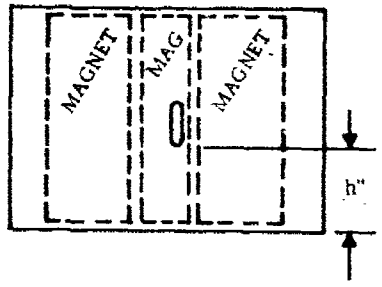

Distance d(IN.)	GAUSS (x k) "h" 1/16	1/8	1/4	3/8	1/2	5/8	3/4	7/8
0	3.3	3.4	3.39	3.39	3.48	3.48	2.98	0.78
1/16	2.9	3.07	3.25	3.27	3.26	3.13	2.45	1.04
1/8	2.67	2.86	3.2	3.2	3.15	3.0	2.32	1.18
3/16	2.62	2.82	3.16	3.19	3.12	2.95	2.35	1.26
1/4	2.67	2.83	3.1	3.1	3.08	2.95	2.4	1.23
5/16	2.9	2.9	3.13	3.1	3.06	3.0	2.7	1.08
3/8	3.32	3.5	3.3	3.2	3.18	3.4	3.47	0.55

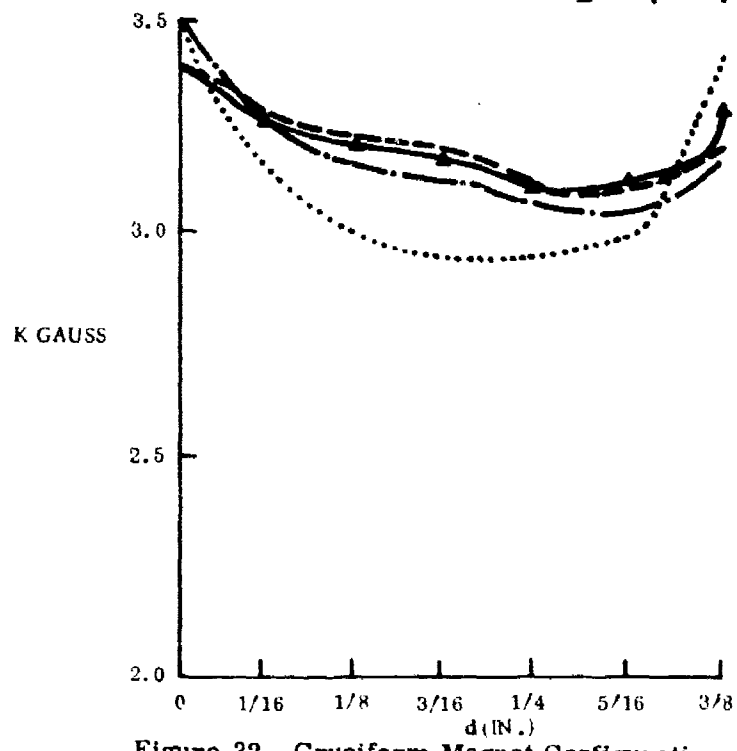

Figure 32. Cruciform Magnet Configuration

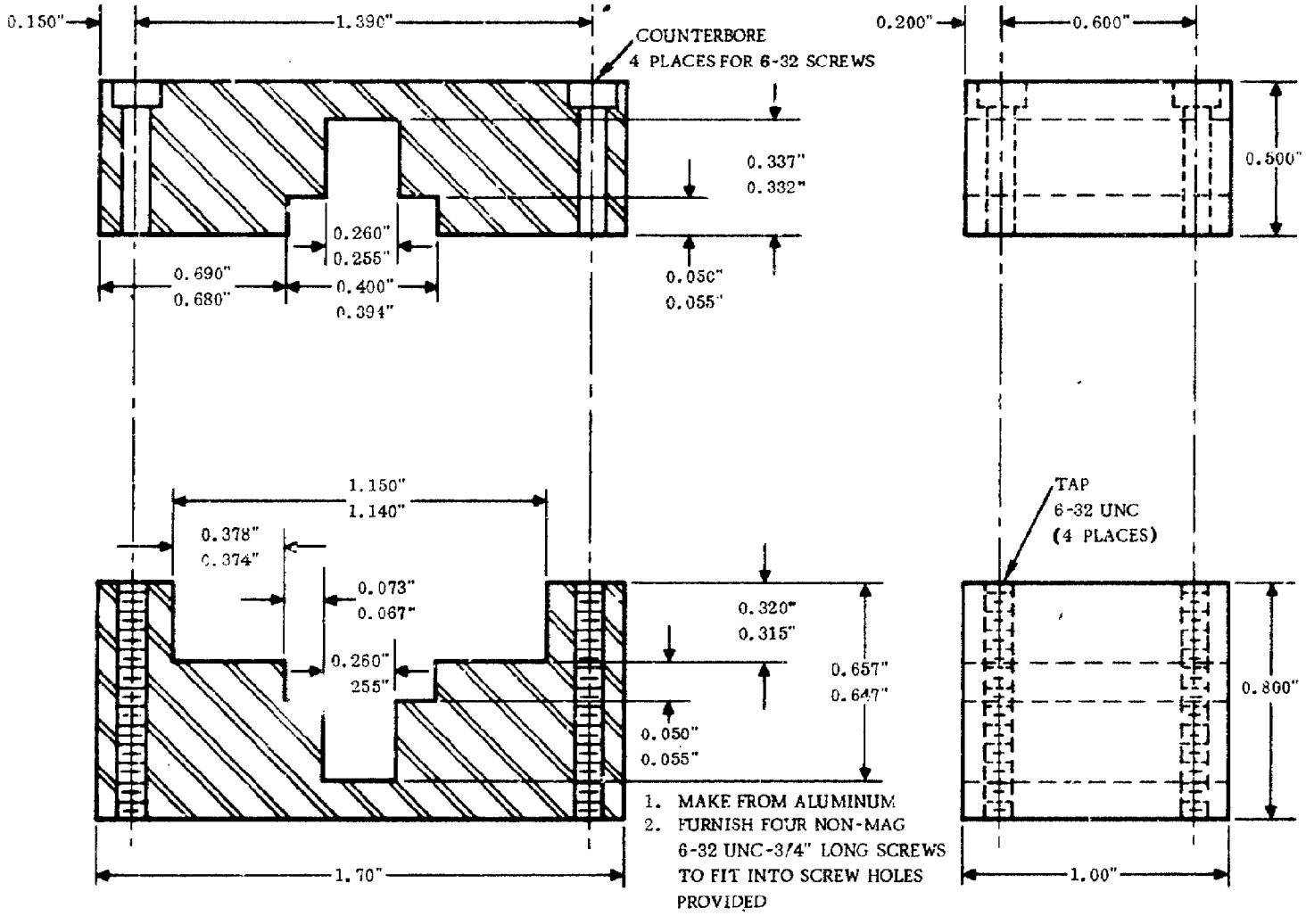

Figure 33. Cruciform Magnet Support

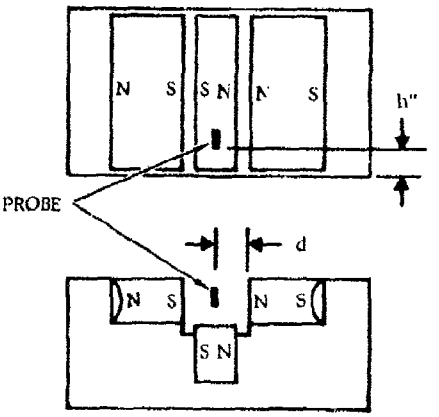

DISTANCE	GAUSS (X 1000)				
	"h"				
"d" (IN.)	.10	.28	.46	.64	.81
0	3.4	3.05	2.83	2.8	3.35
.1	2.35	2.61	2.72	2.45	2.3
.2	2.05	2.45	2.63	2.38	1.8
.3	2.25	2.6	2.65	2.76	1.75
.4	3.18	2.95	2.8	3.0	3.0

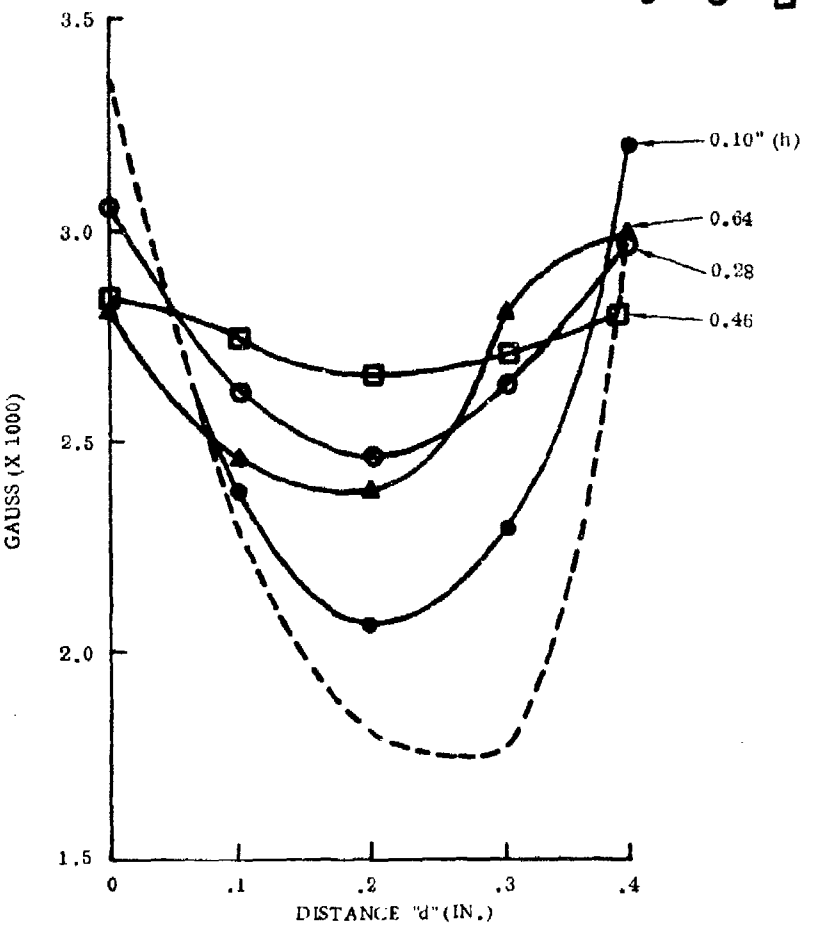

Figure 34. Triple Magnet Deliverable Device

An identical structure made about two months after the first gave good repeatability.

Magnet curving in the Z axis was attempted, but the one configuration tried was unsuccessful. It did however, indicate that further refinement will probably produce results.

k. Five Magnet-Twin Channel Device

In order to increase the bandwidth, a two channel device was constructed which shared one of the field magnets thus requiring five, rather than six magnets. One channel was provided with a fixed airgap, and the other with a variable airgap for field strength/frequency adjustment. The field deflecting magnets were increased in depth from 0.3 in. on the single channel device, to 0.375 in. This had the effect of increasing the level about 300 gauss, but gave a 50 percent increase in field strength variation. Figure 35 shows the results of both the fixed and variable gaps, and Figure 36 shows details of the five magnet structure.

5. MACHINING AND HANDLING

The magnet supplier recommended cutting and grinding samarium cobalt magnets with silicon carbide wheels, slow feed, and lots of coolant. Magnets cut and ground in this manner showed a large number of fine to medium cracks. Changing to diamond for cutting and an Aluminum oxide 60K wheel for grinding, both with fine feed and lots of coolant solved the problem. Machining was recommended in the unmagnetized state, but no problem was encountered with magnetized magnets. Each ground particle would tend to remain and abrade the grinding machine long after the magnets had been ground, but insufficient magnets were ground to prove this.

Samarium cobalt magnets are very brittle. Magnets 0.100 in. thick broke even when packed with polyurethane foam in plastic boxes 1-3/8 x 1-3/8 x 1 in. The extremely strong magnets would twist a plastic box from the hand when approaching another magnet in a box.

Some magnets were supplied with a crack already partly through in the manner of a manufacturing flaw. These would separate or break if cut near the crack. Magnet strength did not appear lessened by the presence of cracks. Small pieces would easily chip from sharp edges. Breakage could easily occur with movement occurring during magnetization. When magnets were improperly bonded to the aluminum magnet structure some magnets were damaged when they broke free after a time.

6. SUMMARY

Magnet configurations were developed having field strengths of 2.5 kilogauss and above, suitable for both dispersive and non-dispersive X-band delay lines.

The two configurations developed have a low weight potential because they require neither magnetic pole pieces nor yokes, only a minimum supporting structure.

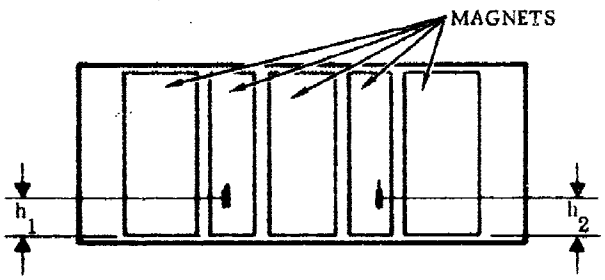

FIXED GAP

DISTANCE	GAUSS (X 1000)				
	"h_1"				
"d_1"	0.1	0.28	0.46	0.64	0.8
.0	3.75	3.7	3.7	3.76	3.44
.1	2.85	3.13	3.2	2.85	2.7
.2	2.21	2.76	2.82	2.65	2.03
.3	2.6	3.05	3.1	3.0	2.4
.4	3.75	3.72	3.64	3.75	3.27

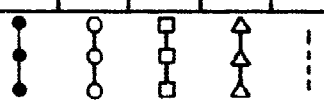

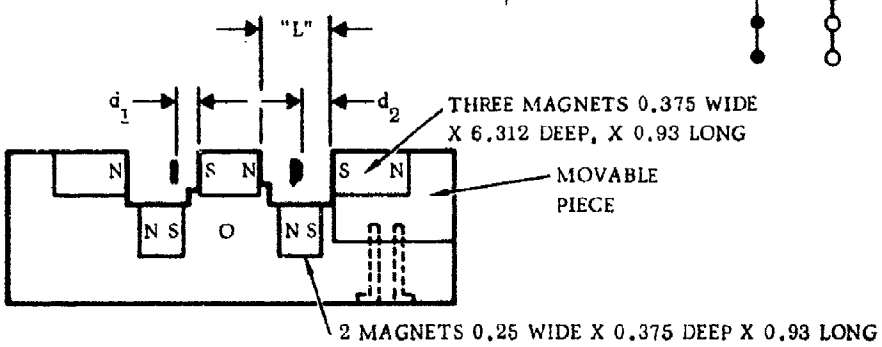

VARIABLE GAP

DISTANCE	GAUSS (X1000)									DISTANCE
	h_2					h_2				
	"L" MIN (.375")					"L" MAX (.460")				
"d_2"	.10	.28	.46	.64	.8	.10	.28	.46	.64	.8	"d_2"
0	3.8	3.83	3.76	3.85	3.54	3.55	3.44	3.35	3.42	3.1	0
1/16	3.25	3.68	3.4	3.76	3.3	2.55	2.92	2.76	2.46	2.77	.06
1/8	2.75	3.17	3.13	3.1	2.65	1.87	2.33	2.35	2.15	1.92	.16
3/16	2.4	2.95	2.85	2.85	2.25	1.9	2.4	2.5	2.35	1.69	.26
1/4	2.4	2.9	2.9	2.77	2.2	2.3	2.8	2.8	2.7	2.04	.36
5/16	2.87	3.15	3.2	3.05	2.4	3.37	3.43	3.48	3.31	3.25	.46
3/8	3.45	3.6	3.6	3.5	3.2						

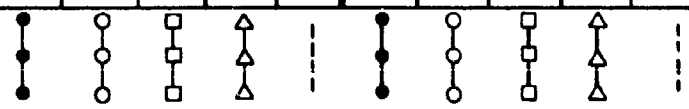

Figure 35. Five Magnet-Twin Channel Device

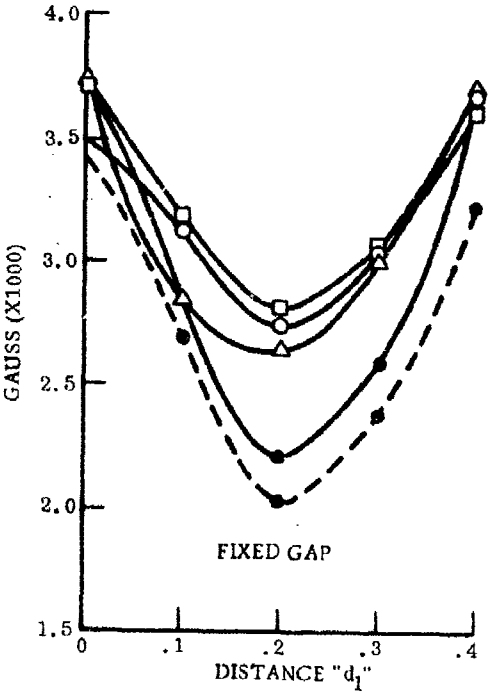

Figure 35. (Cont)

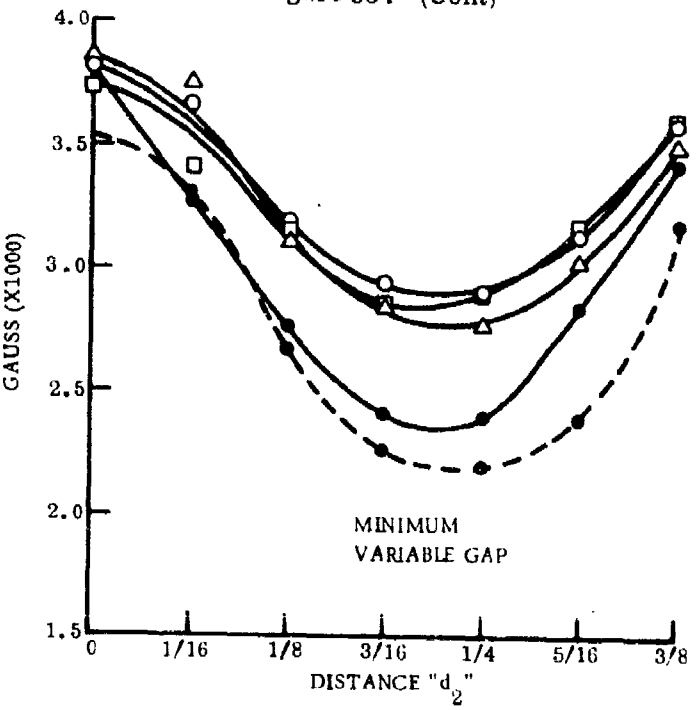

Figure 35. (Cont)

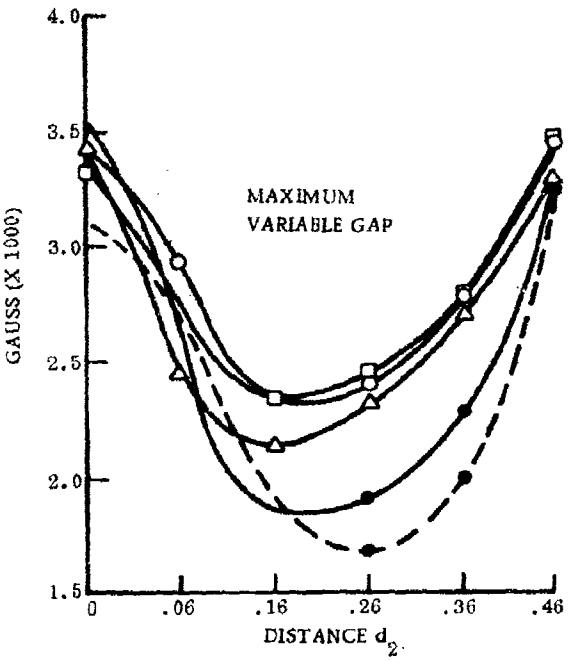

Figure 35. (Concluded)

6. SUMMARY (CONT)

Samarium cobalt magnets can be easily machined in the unmagnetized condition using diamond saws or aluminum oxide 60K grinding wheels, with slow feeds and lots of coolant.

Extreme care must be exercised when handling in order to avoid chipping and breaking. Particular care must be used when magnetizing or when a magnet is near a magnetic surface (or other magnet).

A comparison of highest field strength measured, and field uniformity for the principle configuration tested is shown in Table V. Values given were selected to give the most uniform field for each configuration.

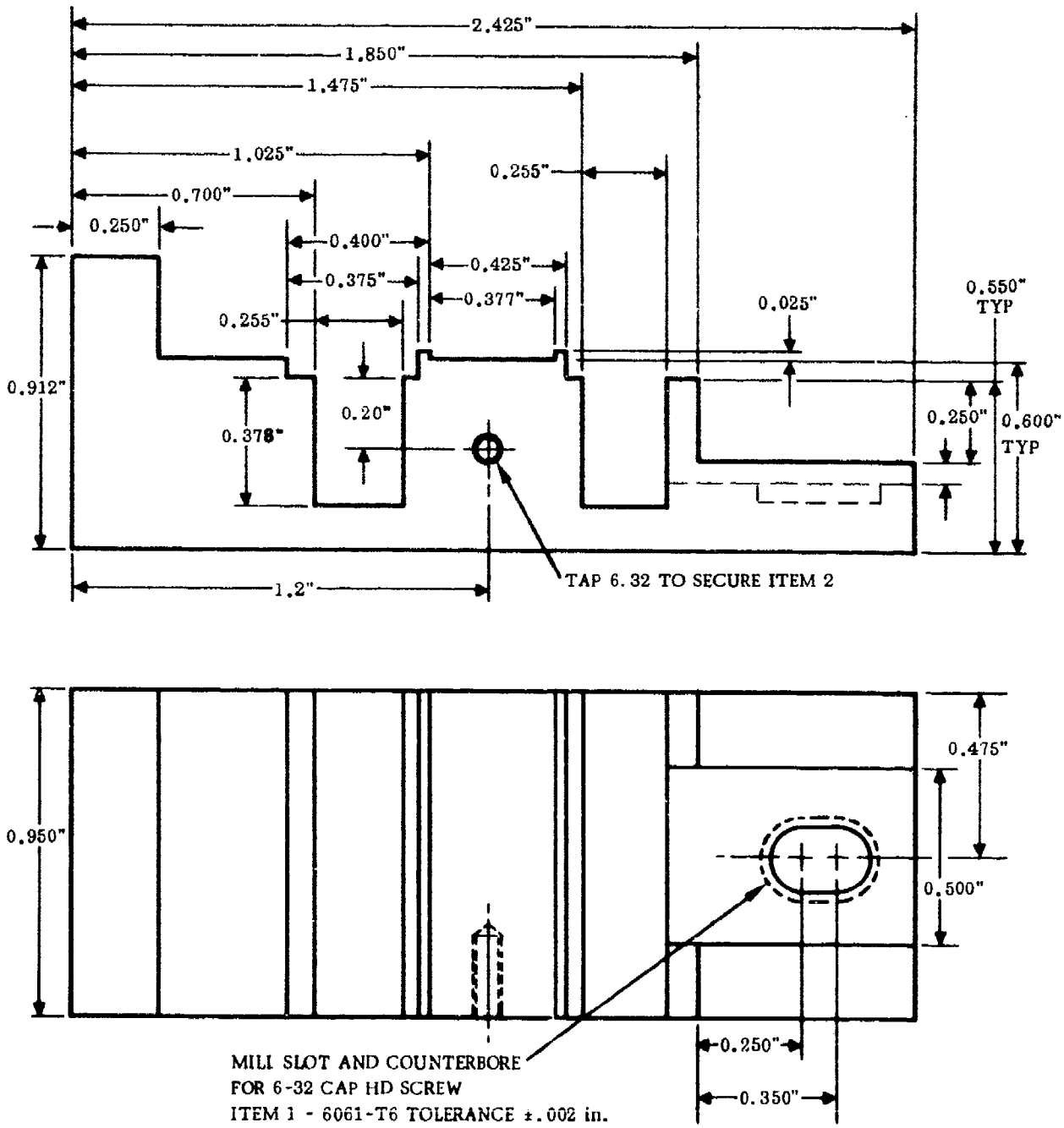

Figure 36. Magnet Structure for Five Magnet Twin Channel Device

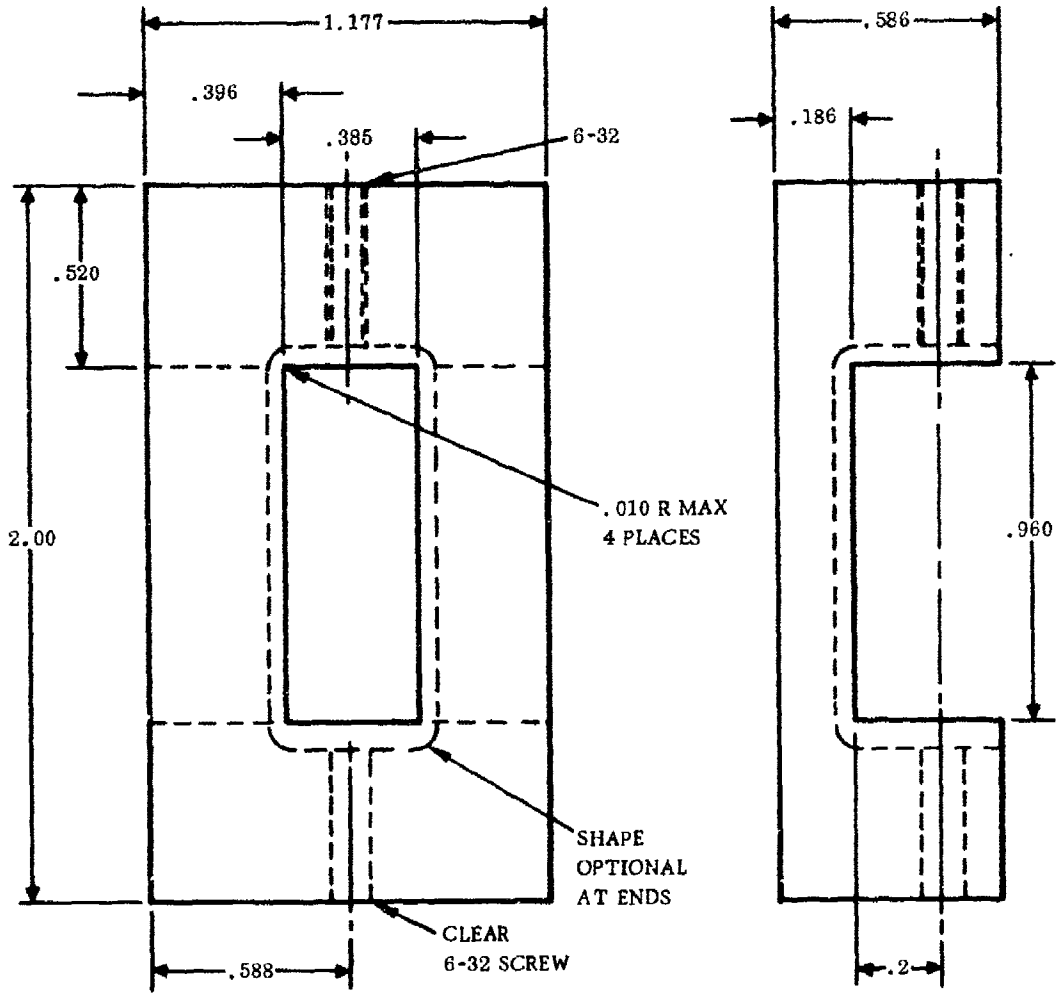

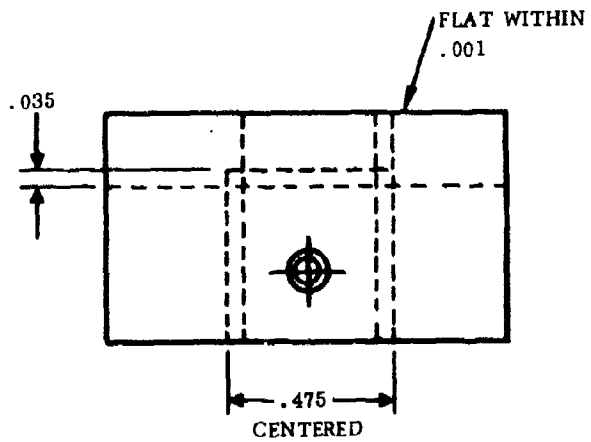

ITEM 2 6061-T6
TOLERANCES ± .002 IN.

Figure 36. (Cont)

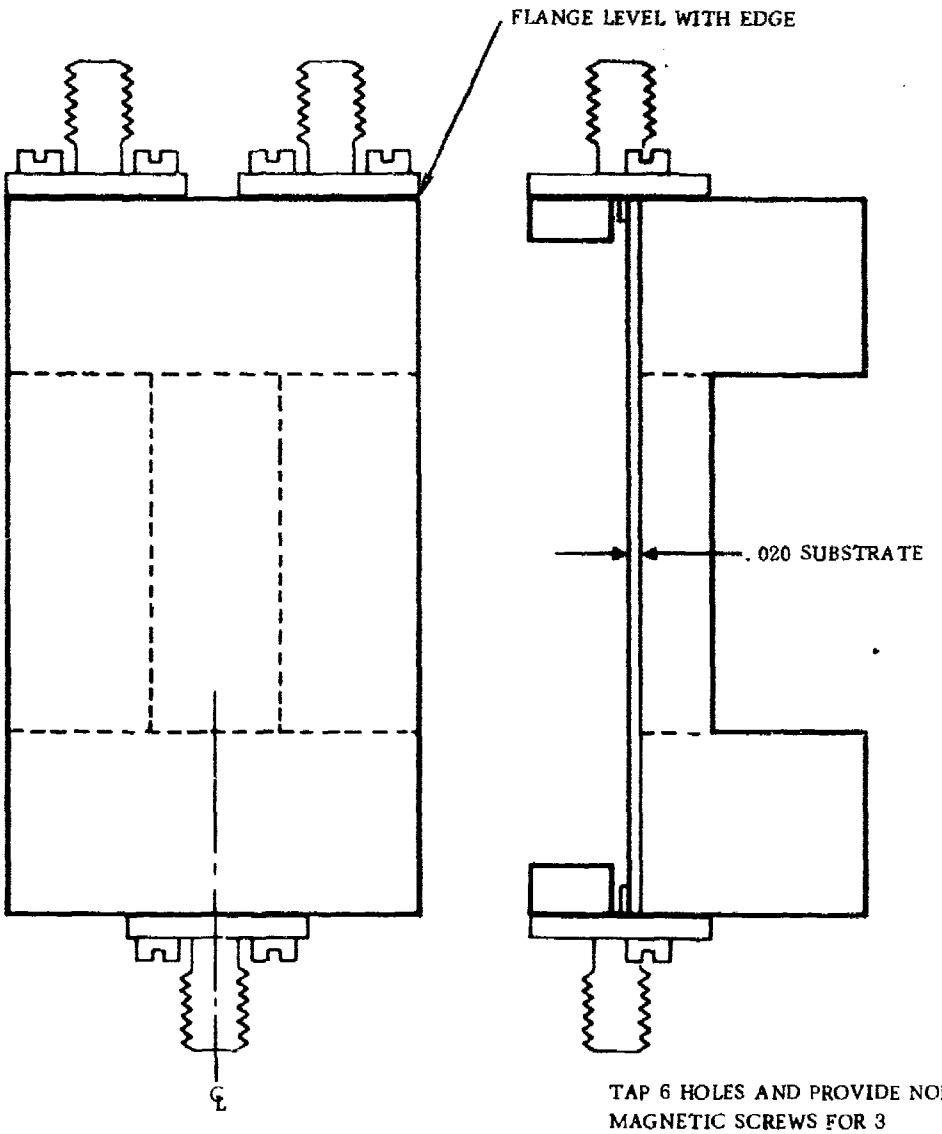

TAP 6 HOLES AND PROVIDE NON-MAGNETIC SCREWS FOR 3 CONNECTORS. CENTRAL CONTACT TO JUST REST ON .020 SUBSTRATE

ITEM 2 (CONT)

Figure 36. (Cont

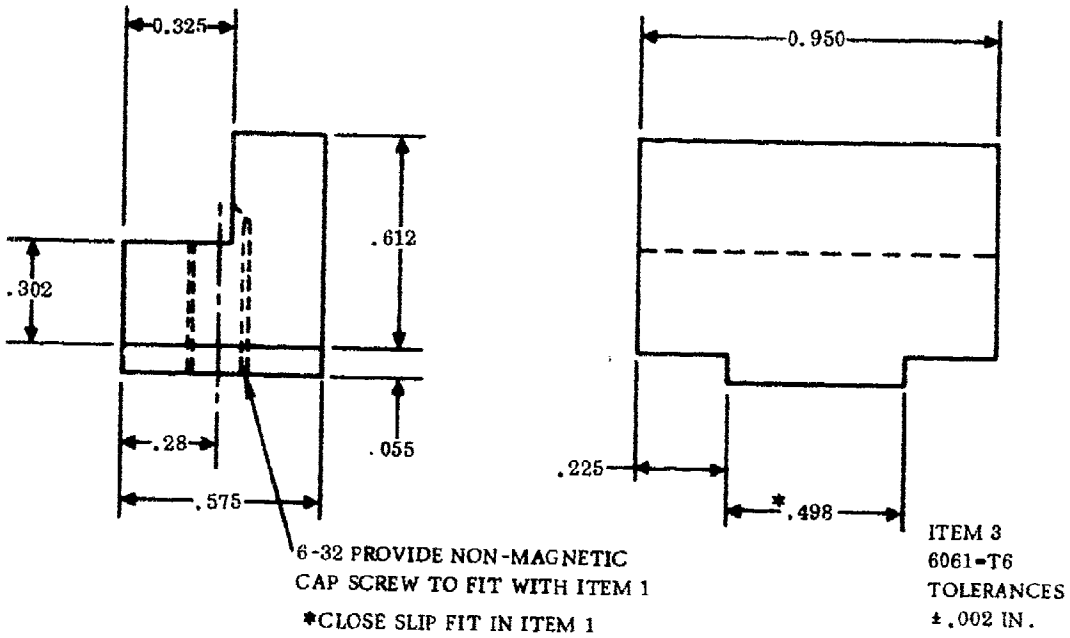

Figure 36. (Concluded)

Table V. Comparison of Various Magnet Configurations

Magnet Configuration	Highest Field Measured (Kilogauss)	Field Uniformity (Kilogauss)	Comment
Single Magnet	1.9	None	No Good
Dual Magnets	3.6	2	Poor Uniformity
Dual Magnets on SiFe Subyoke	1.33	0.11	Field Strength Too Low
Dual Magnets on External SiFe Yoke	4	1.65	Poor Uniformity
Dual Magnets on External 1018 Yoke	3.6	1.66	Poor Uniformity, Heavy
As Above + Y axis magnet shaping	2.56	1.26	Poor Uniformity, Heavy
Triple Magnets on External 1018 Yoke	3.7	0.15	OK, Heavy
Cruciform	3.2	0.25	OK
*Triple Magnet (Modified Cruciform)	2.72	0.34	OK, can probably be improved
*5 Magnet-Twin Channel	3.17	0.32	OK can probably be improved

* Final Selection

SECTION V

X-BAND DEVICES

1. X-BAND NONDISPERSIVE DELAY LINE

X-band nondispersive performance was measured in a three magnet device for two different films. The films were No. 2771-3(2) and No. 2771-3(3) and represented two slices from the same CVD YIG film of 10.5 μm thickness. The microwave circuit consisted of two open circuited transmission lines separated by 0.5 cm on a 20 mil alumina substrate. The circuit is shown in Figure 37. The dc resistivity of the transmission line was initially 20 Ω, but this was reduced to less than 1Ω after electroplating with gold.

The impedance of each port is plotted over the range of 8.5 to 9.5 GHz in Figure 38. As can be seen, the circuit without the presence of the YIG represents an impedance mismatch of greater than 10:1.

The YIG sample No. 2771-3(2) is then placed into the circuit and shifted about until a nondistorted delayed pulse is obtained in a pulse delay set up. Once this was accomplished the impedance of both ports was plotted as shown in Figure 39.

The mismatch is now less than 3:1 for a frequency of 8.415 MHz, which implies a mismatch loss of about 1.2 DB per port, or 2.4 DB total.

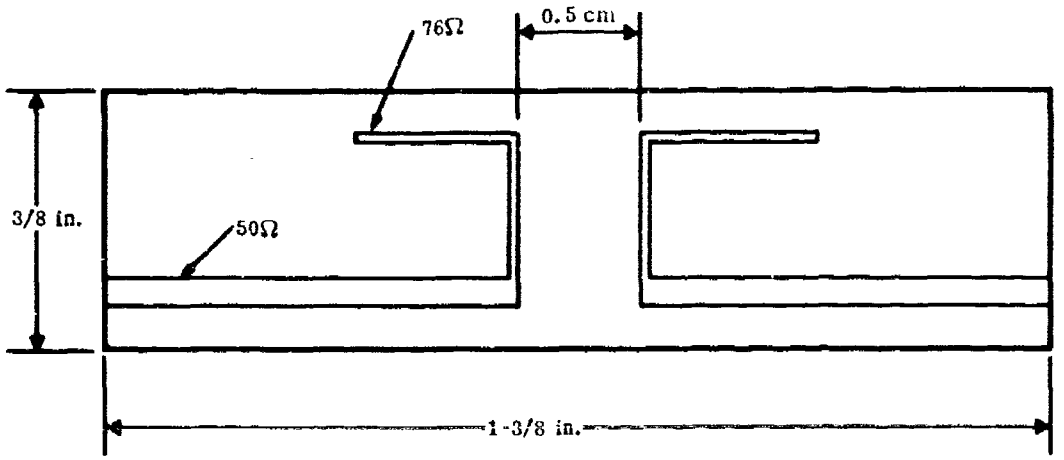

Figure 37. Microstrip Circuit on 20 Mil Alumina

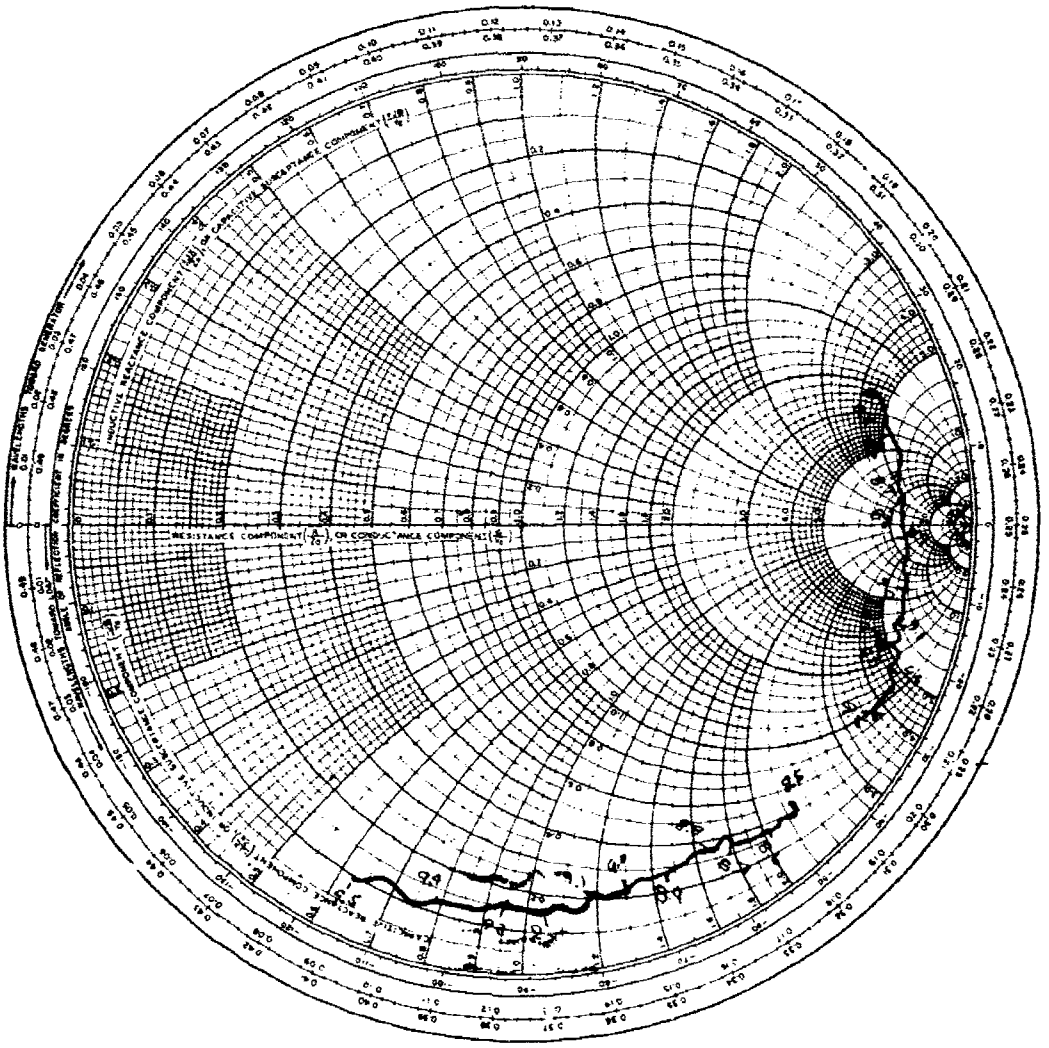

Figure 38. 30 Mil YIG Feed 4.5 cm of Air Line

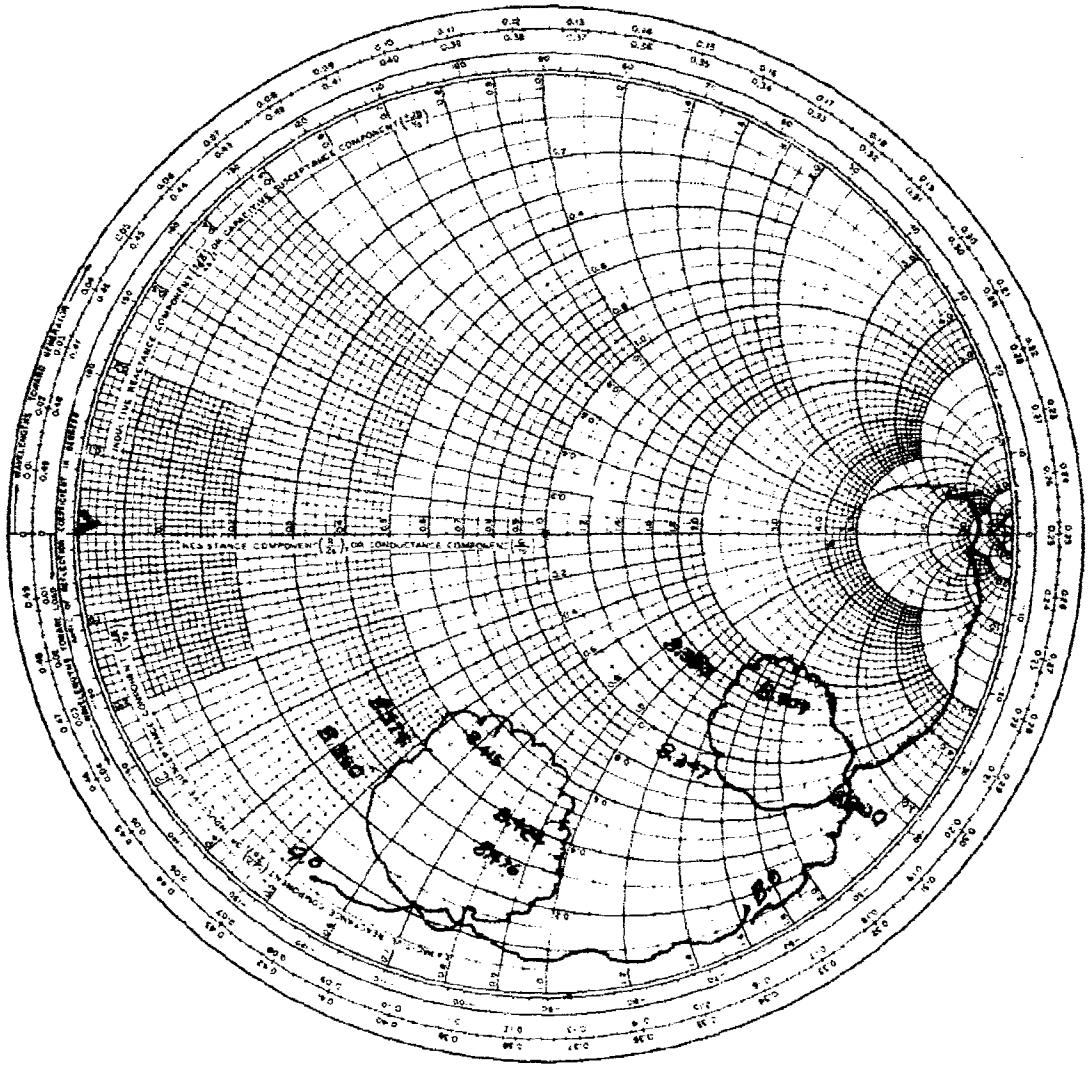

Figure 39. 30 Mil Feed with No. 2771-3(2) YIG and 4.5 cm Air Line

A transmission and phase plot is shown for this device in Figure 40. The amplitude plot shows a minimum insertion loss of 25 DB at 8.385 GHz with a -3 DB bandpass from 8.374 to 8.405, or a bandwidth of 31 MHz. The transmission loss is calculated from the difference of the insertion loss and the mismatch loss as 22.6 DB.

The delay time is calculated from the phase plot by using the relation

$$t = \frac{d\phi}{d_\omega} = \frac{\Delta\phi}{2\pi\Delta f} \quad .$$

Since each vertical sweep represents a $\Delta\phi = \pi$, the same point on every other sweep is 2π, and the above equation becomes

$$t = \frac{2\pi}{2\pi\Delta f_{2\pi}} = \frac{1}{\Delta f_{2\pi}} \ (\text{sec}^{-1})$$

The calculated delay time is shown at the top. As expected, the bandpass occurs in the plateau region of the time dispersion. A total delay of 120 nsec with an excursion of ±6 nsec is obtained. The loss per microsecond is 22.6 DB/120 nsec = 174 DB/μsec, which implies a linewidth of 4.55 Oe. This agrees with the 4.0 Oe measured in a uniform electromagnet at X-band which implies a field uniformity to about 0.5 Oe for the samarium cobalt structure. The feedthrough level is approximately down by 35 DB. Attempts to reduce this level by metal partitions were not successful.

In order to determine the delay repeatability due to sample characteristics, the No. 2771-3(2) was replaced with No. 2771-3(3), a different cut sample from the same YIG deposition, and the parameters were remeasured. Figure 41 shows that the YIG is matched to a ratio of 2:1 (0.5 DB reflection loss), which implies a 1.0 DB mismatch loss. Figure 42 shows the bandpass and phase measurements for this device. The delay is calculated as 125 nsec ± 4 nsec over a 3 DB bandwidth of 45 MHz. A rubber grommet was found to actively suppress feedthrough to about 45 DB.

A comparison of the results is shown in Table VI.

Table VI. Two 10.5 Films at X-Band

Sample No.	Delay per 0.5 cm	Insertion Loss	Bandwidth	Linewidth
2771-3(2)	120 ± 6 nsec	25 DB	31 MHz	4.55 Oe
2771-3(3)	125 ± 4 nsec	20 DB	45 MHz	4.0 Oe

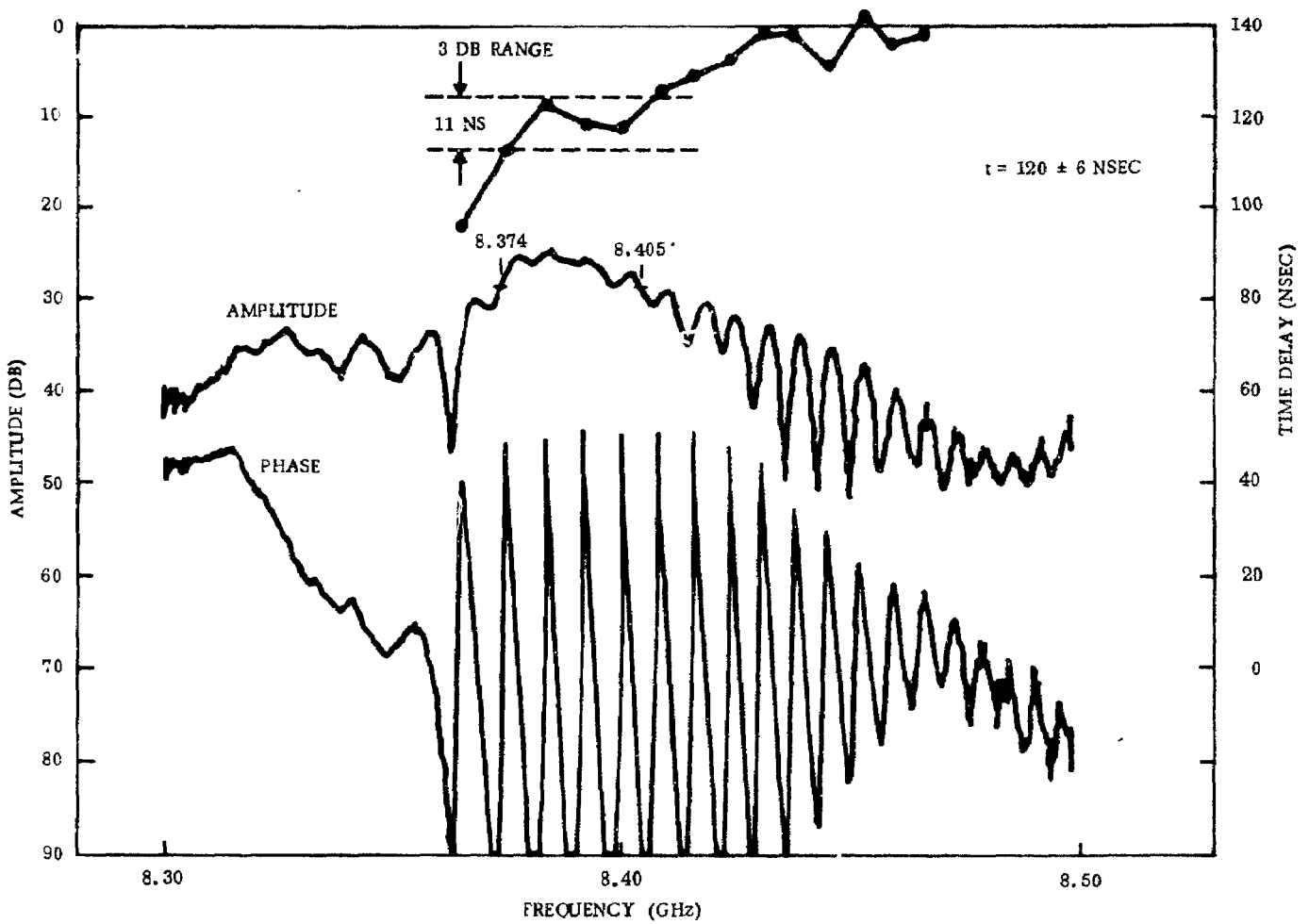

Figure 40. No. 2771-(2) YIG 3 Mil Coupler, 0.5 cm Spaling, 20 Mil Alumina

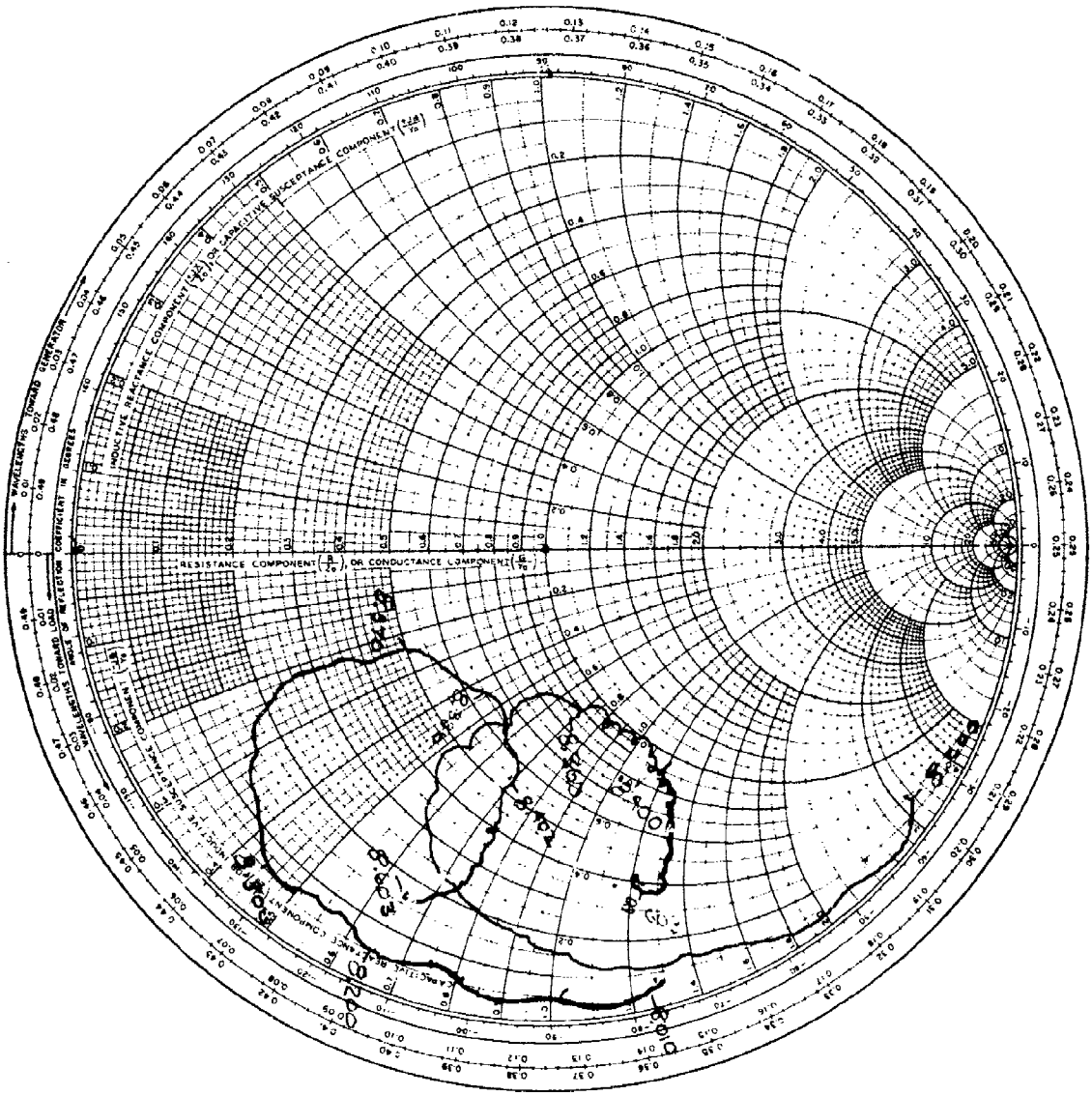

Figure 41. No. 2771-3(3) YIG

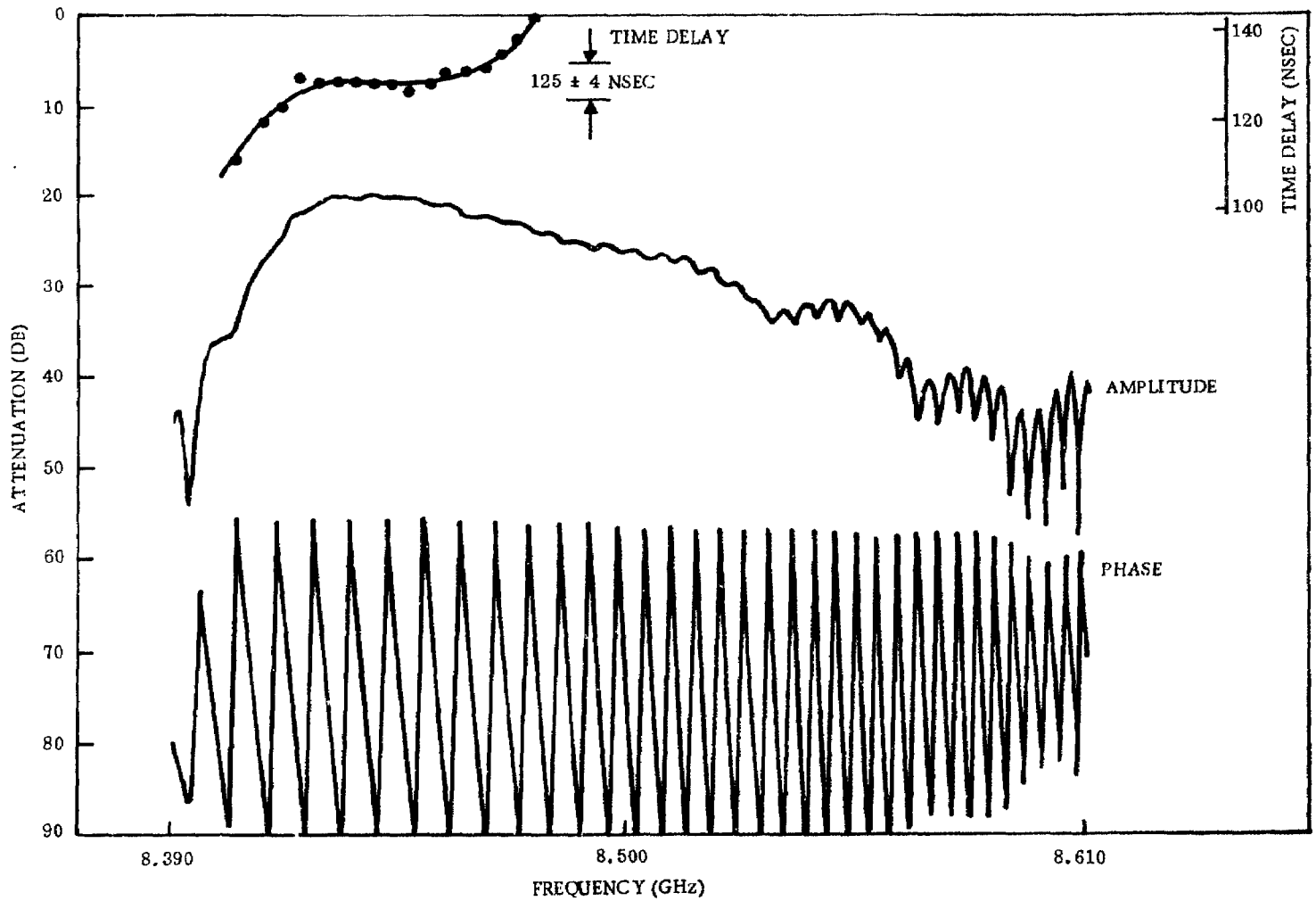

Figure 42. No. 2771-3(3) YIG, 3 Mil Coupler, 0.5 cm Spaling, 20 Mil Alumina, (Rubber Grommet Feedthrough Suppression)

If both films were used in a two channel device, a total bandwidth of 76 MHz would be obtained. The resolution of this bandwith is 14 nsec, which is within the mean errors of the different films. The number of resolvable bits in such a line would be 120 nsec/ 14 nsec = 8, or about double the number in a single channel alone.

2. X-BAND DISPERSIVE DELAY LINE

A dispersive delay line was assembled using the LPE film NRA-403B-3 with a three magnet cruciform assembly and a microstrip line discussed in the previous section. The film was placed onto the circuit and positioned using a pulsed RF generator to serve as a reference for best alignment. Alignment was made in order to obtain minimum insertion loss with some attention to linearity of delay and pulse shape fidelity.

When a minimum loss figure was obtained, the sample was fixed with airplane glue, and a total dispersion characteristic was made. The results for this line are indicated in Figure 43. The dispersion is linear from 8.9 to almost 9.2 GHz with a total differential delay over this range of 175 nsec. This represents a time-bandwidth product of 52.5. The bandpass characteristic is "Taylor" like, as is desirable in a receiver compression line. At the -12 DB points, the line has a bandwidth of 225 MHz and a differential delay of 138 nsec, hence this line can accommodate a chirp with a time-bandwidth product of 31.

Pulse compression was achieved in the device, DDL-EY-3, which was assembled and tested as described above. The compression loop was built around a voltage controlled oscillator which has a linearity of better than ±2 percent. A linear voltage ramp was used to drive the VCO, as is shown in the compression loop schematic (Figure 44). The VCO works over a range of 2.325 to 2.675 GHz and requires mixing with a CW source at about 6.6 GHz to produce the required 9.1 GHz center frequency. This signal was gated and sampled by a directional coupler. The main signal passes through various precision attenuators (for -4 DB and sidelobe measurements) into the YIG dispersive delay line. The compressed pulse is amplified by a low noise amplifier and displayed on a sampling scope.

The spectrum of the chirp is shown in Figure 45. The full bandwidth of the chirp is about 200 MHz, centered at 9.10 GHz. The time display of the chirp is shown on the lower trace of Figure 46, and has a duration of about 150 nsec. This chirp has a time bandwidth product of 30. The chirp pulse is compressed by the YIG DDL and delayed about 250 nsec from the beginning of the input, as shown by the upper trace.

The bandpass of the YIG device is such as to weight the input chirp. Figure 47 shows a detailed view of the sidelobes. Note that this photograph is a double exposure with the second trace being attenuated by 20 DB from the first. Since the main lobe is about even with the sidelobes, it is concluded that sidelobe suppression is 20 DB.

An expanded view of the compressed pulse is given in Figure 48, showing the -4 DB points at the center line of the graticule. At this point, the pulsewidth is almost 8 nsec. This is wider than the 5 nsec, based on the chirp bandwidth, and is attributed to the "Taylor" like bandpass response which is responsible for the sidelobe suppression. Final evidence of this weighting is given in Figure 49 which shows the spectrum at the output of the YIG DDL. Notice that the relatively flat spectrum of the input chirp (Figure 45) has been weighted.

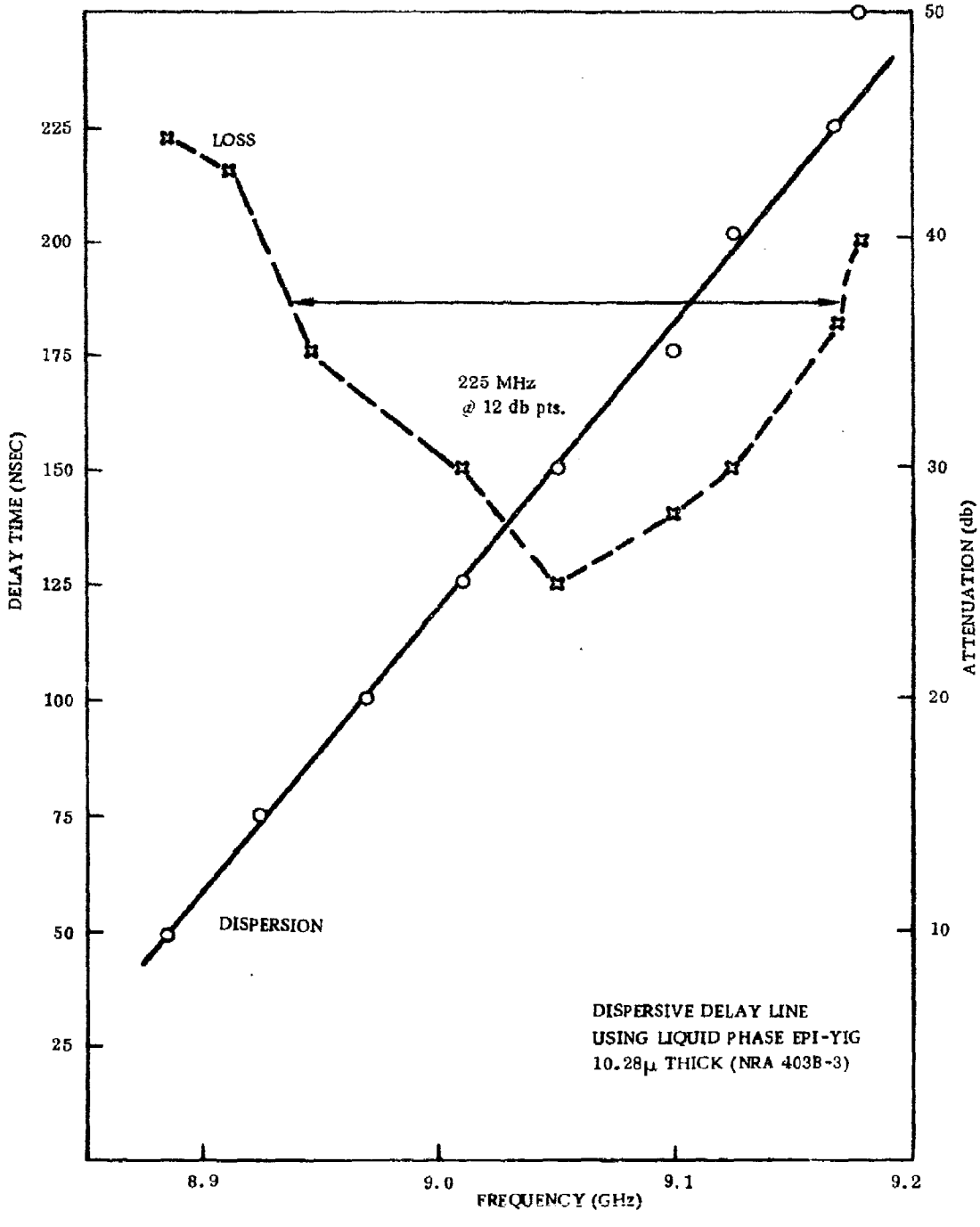

Figure 43. Dispersive Delay Line Using LPE YIG 10.28 μm Thick (NRA 403B-3)

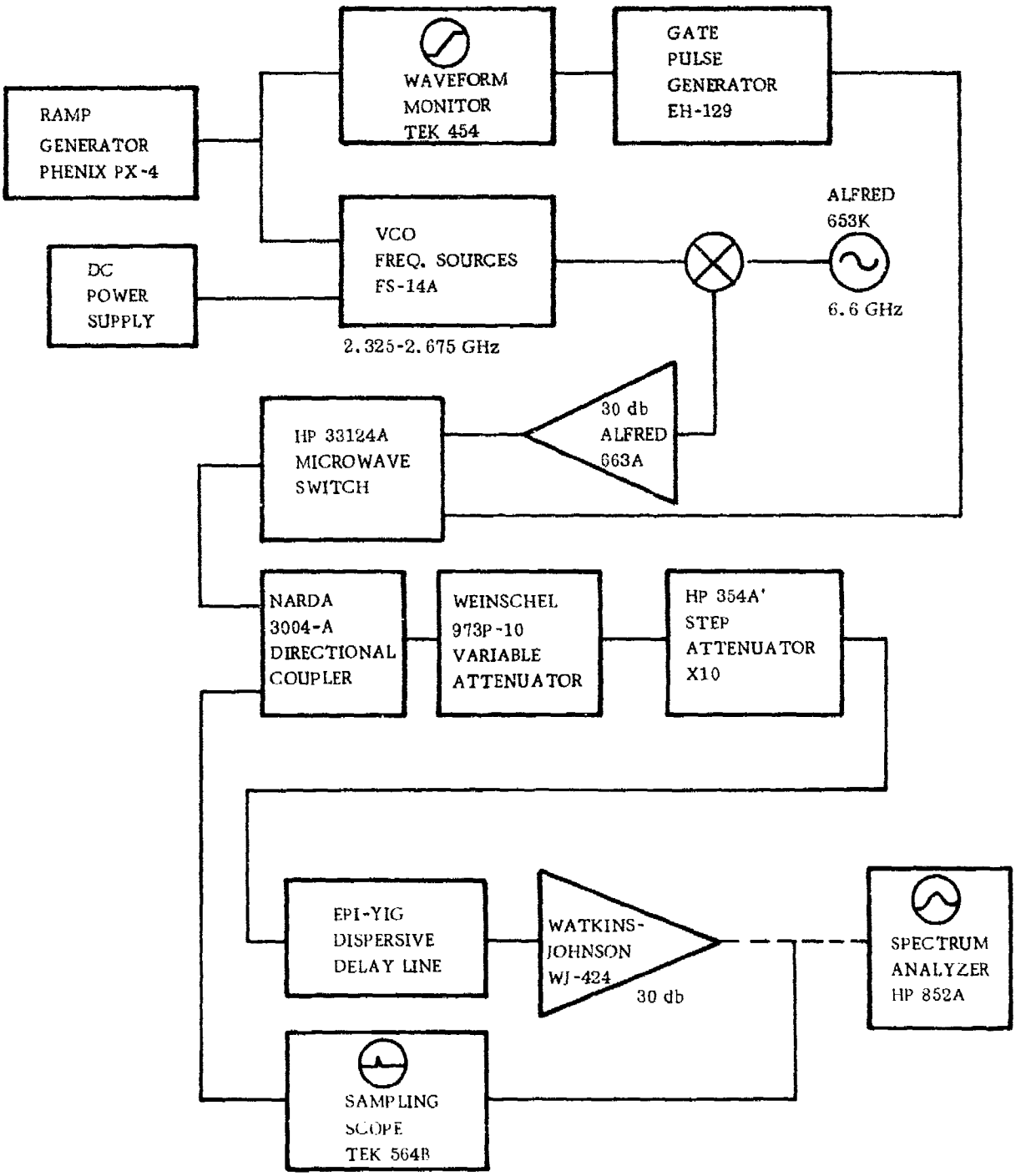

Figure 44. Compression Loop for the X-Band Epitaxial YIG Dispersive Delay Line DDL-EY-3

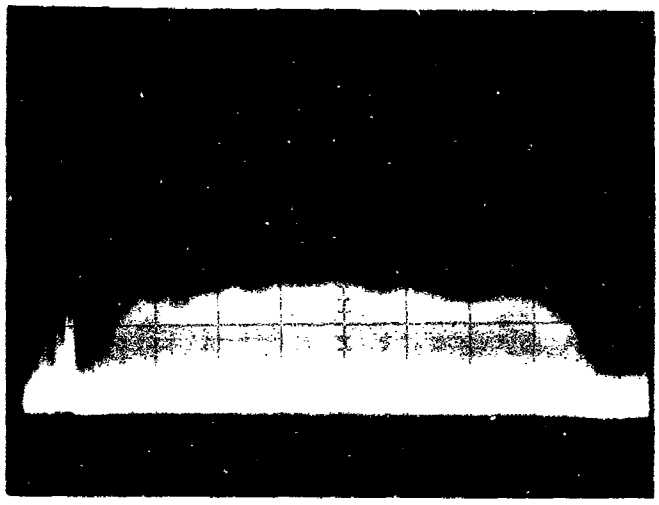

10 db/div. vert.

30 MHz/div. centered at 9.10 GHz horz.

Figure 45. Spectrum of Input Chip

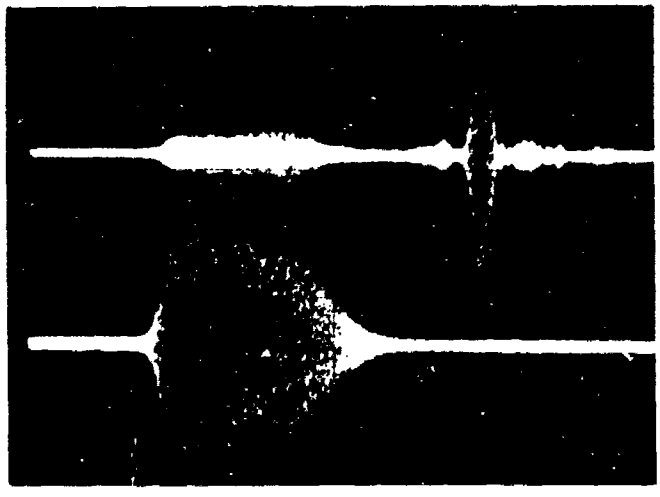

Compressed Pulse on upper trace

Input Chip on lower trace

50 nsec/div. horz.

Figure 46. Time Domain

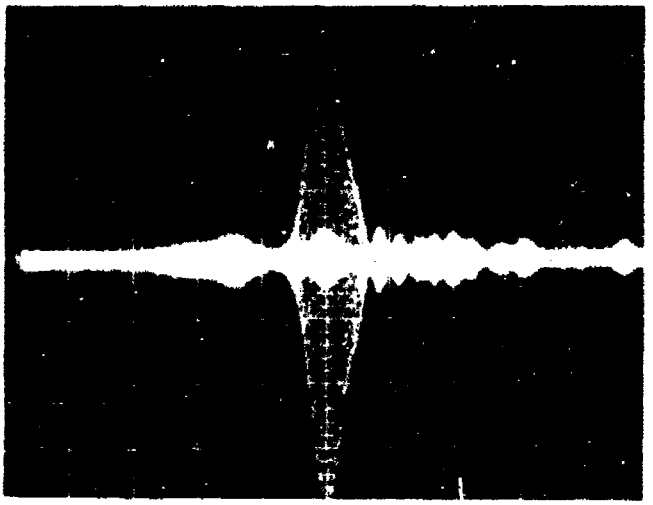

Double exposure of compressed pulse with and without 20 db. attenuation

20 nsec/div. horz.

Figure 47. Side Lobe Level

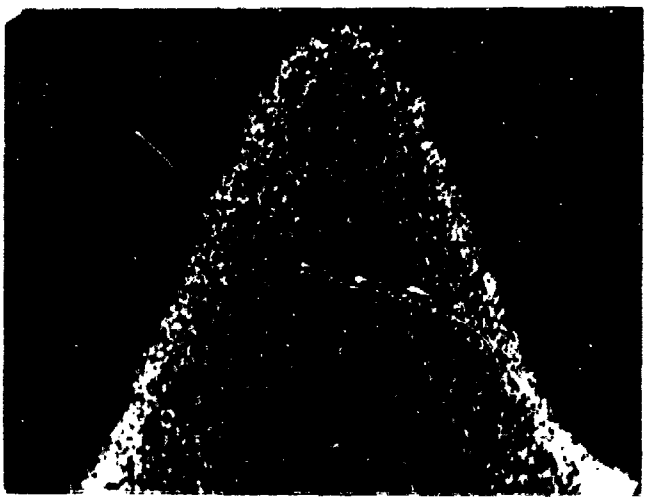

- Expanded View of compressed pulse

2 nsec/div. with -4db. located at center line of graticule. (~8 nsec)

Figure 48. -4 DB Points

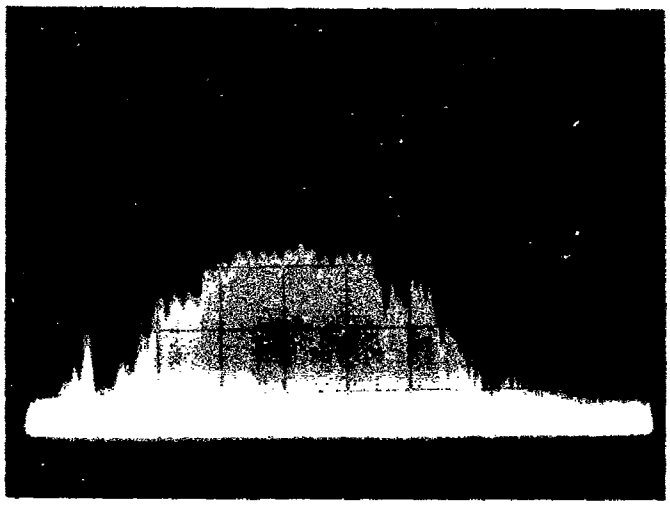

10 db/div. vert.
30 MHz/div, centered at
9.10 GHz horz.

Figure 49. Chip Spectrum Weighted by the Dispersive Delay Line

3. SPECIFICATIONS ON DDL-EY-3

The above line was sent to the contractor as satisfying Task 7 of the original contract. As such it might be of interest to compare the results obtained with those goals originally proposed. This is done in Table VII. Some parameters were missed, namely bandwidth and pulse compression ratio. Others, however, were met or surpassed — center frequency and insertion loss.

Table VII. Specifications on DDL-EY-3

	Goals	Device Performance
Center Frequency	9.0 GHz	9.1 GHz
Bandwidth	1.0 GHz	300 MHz Linear Range (Matched to 200 MHz Chirp)
Pulse Compression Ratio	1000:1	52.5 Linear Range (Matched to 30:1 Chirp)
Attenuation Ripple	2 DB	~2 DB
Insertion Loss	<40 DB	25 DB
Bandpass Response	Unspecified	"Taylor" Weighted
Dispersive Delay	Unspecified	175 nsec (~150 nsec Matched to Chirp)
Delay from Input	Unspecified	0.25 μsec

REFERENCES

1. J. E. Mee, G. R. Pulliam, D. M. Heinz, J. M. Owens and P. J. Besser, Appl. Phys. Lett. 18, 60 (1971).

2. C. D. Brandle and A. J. Valentino, J. Cryst. Growth 12, 3 (1972).

3. H. L. Glass, Mat. Res. Bull. 7, 1087 (1972).

4. C. D. Brandle, D. C. Miller and J. W. Nielsen, J. Cryst. Growth 12, 195 (1972).

5. H. L. Glass, Mat. Res. Bull. 7, 385 (1972).

6. R. F. Belt, J. Appl. Phys. 40, 1644 (1969).

7. J. E. Mee, G. R. Pulliam, J. L. Archer and P. J. Besser, IEEE Trans. Mag-5, 717 (1969).

8. H. J. Levenstein, S. Licht, R. W. Landorf and S. L. Blank, Appl. Phys. Lett. 19, 486 (1971).

9. J. W. Nielsen, "Recent Developments in Crystal Growth from High Temperature Solutions," presented at the All Soviet Union Conference on Crystallography, September 1972.

10. G. W. Roland, Mat. Res. Bull. 7, 983 (1972).

11. E. A. Giess, B. E. Argyle, D. C. Cronemeyer, E. Klokholm, T. R. McGuire, D. F. O'Kane, T. J. Plaskett and V. Sodagopon, AIP Conf. Proc. 5, 110 (1972).

12. E. A. Giess, J. D. Kuptsis and E. A. D. White, J. Cryst. Growth (to be published).

13. W. L. Bongianni, "Epitaxial YIG Microwave Circuits," AFAL-TR-71-275, September 1971.

14. W. L. Bongianni, J. Appl. Phys. 43, 2541 (1972).

15. L. K. Brundle and N. J. Freedman, Electronics Letters 4, 132 (1968).

16. J. D. Adam, Electronics Letters 6, 718 (1970).

17. P. J. Besser, et al, "Epitaxial Growth of Ferrimagnetic Garnets," Contract No. F33615-69-C-1520.

18. G. F. Dionne, J. Appl. Phys. 43, 1221 (1972).

19. J. B. Merry and J. C. Sethares, "Low Loss Magnetostatic Surface Waves at Frequencies Up to 15 GHz," to be presented at 1973 Intermag Conference in Washington, D.C.

UNCLASSIFIED

Security Classification

DOCUMENT CONTROL DATA - R & D

(Security classification of title, body of abstract and indexing annotation must be entered when the overall report is classified)

1. ORIGINATING ACTIVITY (Corporate author)

North American Rockwell Corporation
Electronics Group
Anaheim CA 92803

2a. REPORT SECURITY CLASSIFICATION: Unclassified

2b. GROUP:

3. REPORT TITLE

MICROWAVE FILTERS AND DELAY LINES

4. DESCRIPTIVE NOTES (Type of report and inclusive dates)

Final Report 8 May 1972 - 29 December 1972

5. AUTHOR(S) (First name, middle initial, last name)

W. L. Bongianni
D. M. Heinz
L. Needham

6. REPORT DATE	7a. TOTAL NO. OF PAGES	7b. NO. OF REFS
April 1973	70	19

8a. CONTRACT OR GRANT NO.	9a. ORIGINATOR'S REPORT NUMBER(S)
F33615-72-C-1760	C72-585/501
b. PROJECT NO.	
c.	9b. OTHER REPORT NO(S) (Any other numbers that may be assigned this report)
d.	AFAL-TR-73-72

10. DISTRIBUTION STATEMENT

"Distribution limited to U. S. Government Agencies only; test and evaluation results reported; (April 1972). Other requests for this document must be referred to AFAL/TEM, Wright-Patterson AFB, OH 45433."

11. SUPPLEMENTARY NOTES	12. SPONSORING MILITARY ACTIVITY
	Air Force Avionics Laboratory Wright-Patterson Air Force Base Ohio 45433

13. ABSTRACT

The significance of this research and development to the Air Force derives from the need for small, lightweight solid state integrated circuit devices suitable for signal processing applications at Microwave frequencies. The work covered by this report was directed specifically at such devices operating at X band (8.0 to 12.4 GHz). The performance improvement was accomplished by improving the quality of epitaxial YIG films, increasing the knowledge of magnetostatic wave propagation in dielectric layered structures, and utilizing high energy product samarium cobalt magnets. During the period covered by this contract several devices were built and evaluated. These were:

1. A nondispersive delay line at 8.425 GHz with a delay of 124 nsec, an insertion loss of 20 dB, and a bandwidth of 45 MHz;
2. A dispersive delay line operating at 9.1 GHz with a 300 MHz linear dispersion of 175 nsec of differential delay. This device compressed a linear chirp by a factor of 30:1 and weighted the adjacent sides lobes to -20 dB
3. A two tap delay line having a nondispersive delay of 50 nsec and 80 nsec.

The success of these devices in terms of size and operating frequency represents a considerable increase in the state of the art. For the first time, the rf signal designer has the opportunity to perform signal processing at radar signal frequencies, with devices which are compatible with Gunn and IMPATT solid state signal sources.

DD FORM 1 NOV 1473

UNCLASSIFIED

Security Classification

14 KEY WORDS	LINK A		LINK B		LINK C	
	ROLE	WT	ROLE	WT	ROLE	WT
Epitaxial YIG						
Magnetostatic Wave						
Dispersive Delay Line						
Nondispersive Delay Line						
Magnetic Wave Devices						
Magnetostatic Mode in a Dielectric Layered Structure						